Issues Regarding a Complete Computational Model of a Hall Thruster from the Acceleration Channel through the Plume

by

Salma Qarnain

B.S. Mechanical Engineering with Secondary Major in Aeronautics and
Astronautics, Stanford University, 1996

Submitted to the Department of Aeronautics and Astronautics
in partial fulfillment of the requirements for the degree of

Master of Science in Aeronautics and Astronautics

at the

MASSACHUSETTS INSTITUTE OF TECHNOLOGY

May 1998

Author ....
Department of Aeronautics and Astronautics
May 22, 1998

Certified by ....
Manuel Martinez-Sanchez
Professor
Thesis Supervisor

Accepted by ....
Jaime Peraire
Chairman, Department Graduate Committee

Issues Regarding a Complete Computational Model of a Hall Thruster from the Acceleration Channel through the Plume

by

Salma Qarnain

Submitted to the Department of Aeronautics and Astronautics
on May 22, 1998, in partial fulfillment of the
requirements for the degree of
Master of Science in Aeronautics and Astronautics

Abstract

Two- and three-dimensional computational models describing both the internal and external physics of Hall thrusters have been developed at the Massachusetts Institute of Technology. Integration of these models would result in a single, stand-alone application characterizing thruster physics from the thruster interior through the plume region. The application would enhance the spacecraft design process by providing engineers with the ability to predict thruster performance and damage to the craft from plume-spacecraft interactions. This thesis represents the first attempt at consolidation of the internal and external models, exploring the issues critical to integration.

The external model has been enhanced to include a correction to the sputtering yield rate for its surface interaction model and has been tested while varying the source input. Results suggest that the two models can be combined; however, a large amount of reconstruction may be needed for seamless integration.

Thesis Supervisor: Manuel Martinez-Sanchez
Title: Professor

Acknowledgments

I'd like to thank the following people for their support through this work and for helping me to achieve all that I set out for myself and then some.

First, I thank my two thesis advisors. Both have been an inspiration in the pursuit of my degree and models for my career in aerospace. I thank Professor Hastings for his support throughout my first year at MIT and thank Professor Martinez-Sanchez for taking me under his auspice and allowing me the freedom to decide when I was indeed finished with this thesis.

On a more personal note, many thanks to my parents for granting me the opportunity for an amazing education and supporting all my endeavors. Although I did not choose medicine as my field of study, I am convinced that the world is better for it. Who would want a surgeon who instead of concentrating on the patients would always gaze upwards and have her eyes on the stars?

For seeing me through the last couple of years and teaching me to play hockey Canadian style, I profusely thank Sean May. His support has been second-to-none. It is difficult to express how he has brought joy to my life; I simply hope he knows how much.

This page would verily be incomplete without thanking Jarett Dobbins, who selflessly always looked out for my best interests, for his endless support, encouragement, and advice.

I thank the SSL lab members and MIT students for exemplifying what camaraderie is all about: to David Oh, Mike Fife, James Szabo, and Angie Kelic for not looking bothered by my barrage of questions; to Raymond Sedwick and Graeme Shaw for guidance and putting me back on track when I wandered off course; to Graeme whose willingness to give me a smile and to help made this thesis a pleasure to work on; to Wendy Wong, Emerson Quan, and Ankur Garg who have made my time at MIT something I'll not forget.

And finally, a special thank you goes out to SharonLeah Brown for no one event in particular but just for making my life in the lab easier.

This work was sponsored by the Air Force Office of Scientific Research under contract number 97-NA-320, An End-to-End Model of a Hall Thruster. Contract monitor was Mitat Birkan.

"She's an unemployed aeronautical engineer who has spent some time in and out of mental institutions." – Agent Scully, *The X-Files*

"They are scientists. Common sense just gets in their way." – *Sliders*

Contents

1 Introduction **11**

1.1 Previous Modeling Research 14

1.1.1 Acceleration Channel Modeling 14

1.1.2 Plume Modeling 14

1.2 Objective of this Research 15

2 Fundamental Theory **16**

2.1 Hall Thruster Operation 16

2.2 Computational Schemes 17

2.2.1 Particle-In-Cell 17

2.2.2 Direct Simulation Monte Carlo 18

2.2.3 Acceleration Channel Model 19

2.2.4 Plume Model 19

3 Integration Issues **23**

3.1 Physics Issues 23

3.1.1 Source Model 23

3.1.2 Sputtering Model 27

3.1.3 Sensitivity Analysis 30

3.2 Computer Science Issues 32

3.2.1 Automatic Source Model Generation 32

4 Results and Discussion **38**

4.1 Source Model 38
4.1.1 Plasma Oscillations 38
4.1.2 Ion Energy 39
4.1.3 Ionization 42
4.1.4 Exit Plane Distribution 43
4.2 Sputtering Model 46
4.3 Sensitivity Analysis 48

5 Conclusions 63
5.1 Summary of Results 63
5.2 Short-Term Recommendations 65
5.2.1 Source Model 65
5.2.2 Sputtering Model 65
5.2.3 Integration 66
5.3 Long-Term Recommendations 66
5.4 Summary 66

Bibliography 68

List of Figures

2-1 Hall thruster operation. 22

2-2 Schematic of a typical Hall thruster. 22

3-1 Current density measured 4 mm from thruster exit. [12] 33

3-2 Simulated ion flux at thruster exit. 33

3-3 RPA energy distribution taken 50 cm from thruster exit. [Marrese/Gallimore] $P = 5.2 \times 10^{-5}$ Torr 34

3-4 Simulated RPA energy distribution taken 60 cm from thruster exit. $T_i = 34.0$ eV, $P = 2.2 \times 10^{-6}$ Torr 34

3-5 Sputtering yields in keV region as a function of angle of incidence [2]. 35

3-6 Sputtering yield for $Xe^+ \rightarrow Cu$ at 550 eV as a function of angle of incidence [25]. 35

3-7 Sputtering yield for $Xe^+ \rightarrow Cu$ at 1.55 keV as a function of angle of incidence [25]. 36

3-8 Sputtering yield for $Xe^+ \rightarrow Cu$ at 30 keV as a function of angle of incidence [25]. 36

3-9 Domain of analysis for sensitivity calculations. Note: baseline source and sputtering models lie at the origin. 37

4-1 RPA energy distribution taken 1 m from thruster exit. [1] 50

4-2 RPA energy distribution taken 50 cm from thruster exit. [Marrese/Gallimore] $P = 5.2 \times 10^{-5}$ Torr (Figure reprinted here for convenience.) 50

4-3 Simulated RPA energy distribution taken 60 cm from thruster exit. $T_i = 34.0$ eV, $P = 2.2 \times 10^{-6}$ Torr (Figure reprinted here for convenience.) 51

4-4 Simulated RPA energy distribution taken 60 cm from thruster exit. $T_i = 3.4$ eV, $P = 2.2 \times 10^{-6}$ Torr 51
4-5 Comparison of simulated RPA data with and without double ionization. ($z = 0.6$ m) 52
4-6 Comparison of simulated RPA data with and without double ionization at large angles from the thruster centerline. ($z = 0.6$ m) 52
4-7 Comparison of simulated current density with and without double ionization. ($z = 0.6$ m) 53
4-8 Sputtering of silver. Double ions not included. 53
4-9 Baseline sputtering of silver. 54
4-10 Curve fit of data sampled 4 mm from the exit plane. 54
4-11 Curve fit of data sampled 4 mm from the exit plane minus one data point. 55
4-12 Cumulative distribution functions created from ion current density. . 55
4-13 Cumulative distribution functions shown for $r = 0.028 - 0.037$ m. . . 56
4-14 Comparison of Fife and Gavryushin ion current density distributions 4 mm from thruster exit. 56
4-15 Comparison of Fife and Gavryushin beam divergence angle distributions 4 mm from thruster exit. 57
4-16 Comparison of Fife and Gavryushin cumulative distribution functions. 57
4-17 Baseline configuration of satellite. Includes bus, yoke, and array. . . . 58
4-18 Distribution of angle of incidence on all surfaces of satellite. 58
4-19 Baseline sputtering of silicon. 59
4-20 Worst-case sputtering of silver. 59
4-21 Worst-case sputtering of silicon. 60
4-22 Sputtering of silver using Yamamura model for angle of incidence dependence. 60
4-23 Sputtering of silicon using Yamamura model for angle of incidence dependence. 61

4-24 Sputtering of silver using Fife ion current density and beam divergence angle distributions 4 mm from exit. Sputtering angular dependence not included. 61

4-25 Sputtering of silver using Fife ion current density and beam divergence angle distributions 4 mm from exit. Sputtering angular dependence is included. 62

4-26 Sputtering of silicon using Fife ion current density and beam divergence angle distributions 4 mm from exit. Sputtering angular dependence is included. 62

List of Tables

2.1 SPT-100 Nominal Operating Conditions [16] 17

2.2 Collision cross sections for collisions considered in the plume model. [16] 21

3.1 Fits for sputtering yield of normally incident particles, Equation 3.4, for silver, silicon, and quartz. [20] 28

Chapter 1

Introduction

Until recently, the exploration of space has relied upon chemical thrusters to propel satellites and spacecraft into the depths of the unknown. The space industry is now seeing a new generation of electric propulsive devices to accomplish the same tasks while reducing mission cost in the form of Hall thrusters.

Although developed in the 1960's, Hall thruster technology was abandoned in the Western world in favor of higher specific impulse (Isp) ion engines. The former Soviet Union, however, continued its research and eventually flew operational Hall thrusters in the 1980's. The end of the Cold War era fostered an atmosphere for renewed technical communication between Western and Soviet scientists, rekindling Western interest in Hall thrusters. Thus, Western engineers are now demanding a detailed understanding of Hall thrusters in order to incorporate them into near-future satellite programs.

The numerous benefits of electric propulsion (EP) have placed the Hall thruster at the forefront of space propulsion research. Conventional chemical thrusters produce thrust through the thermodynamic expansion of gas generated by chemical reactions. Thus, chemical thrusters are limited in the maximum thrust that can be achieved by the maximum amount of energy which can be extracted from the reaction. This limitation does not exist for electric propulsion devices. High thrust can be achieved given enough power.

Yet, the real benefit of EP devices lies in the reduction of propellant used per maneuver. The reduction of propellant leads to a reduction in mass carried on board. Since the launch cost is driven by the mass carried, the less satellite wet mass, the lower the overall cost of the mission.

The amount of propellant used in a maneuver is given by the rocket equation:

$$\frac{M_p}{M_o} = 1 - e^{\frac{-\Delta V}{gIsp}} \tag{1.1}$$

where M_p is the propellant mass, M_o is the initial mass of the spacecraft, ΔV is the impulse required, and Isp is the specific impulse of the thruster. As can be seen, as $Isp \rightarrow \infty$, $M_p \rightarrow 0$. Therefore, a higher Isp results in less propellant mass used in the maneuver. However, due to power constraints, a higher Isp also implies lower thrust output:

$$P = \frac{FgIsp}{2\eta}. \tag{1.2}$$

Here, P is the power required, F is the thrust force, and η is the efficiency.

Applications which would benefit from such low-thrust, high Isp EP devices include stationkeeping, orbital maneuvers, plane changes, deorbit, deployment, and possibly, interplanetary and interstellar exploration.

Hall thrusters have recently garnered much attention because their operating Isp range is nearly optimal for north-south stationkeeping. Consequently, Hall thrusters are currently being actively marketed for use on Western satellites.

In August of 1997, Hughes Space and Communications introduced a xenon ion engine on a commercial satellite, PanAmSat 5, for east/west stationkeeping. Their Galaxy 8-I satellite, launched in December, is the first commercial satellite to make use of the ion engines for complete attitude control. The mass saving allowed for the accommodation of additional communications payload. [6]

Commercial systems utilizing Hall thrusters are not far behind. Currently, four geostationary Russian satellites are equipped with SPT-100's for north/south and east/west stationkeeping. SPT-100's will also be aboard Aerospatiale's Stentor telecommunications technology satellite in 2000. Space Systems/Loral is just one of many US companies developing its Hall thruster technology base. [19]

NASA, the Ballistic Missile Organization (BMDO), and the Naval Research Laboratory (NRL) have also been preparing Hall thrusters for flight in 1998 for the Russian Hall Effect Thruster Technology (RHETT) program. The second stage in the program provided the propulsion system hardware for the NRL's Electric Propulsion Demonstration Module, the first Western flight of a Hall thruster system. [21]

Recently, experimental Hall thruster characterization has been a hot topic. Techniques such as mass and emission spectrometry and laser-induced fluorescence are used to obtain species-specific information. This information includes particle velocity, flux, temperature, density, and angular distribution. These methods are, however, both expensive and difficult to perform [7].

Yet, it is imperative that satellite designers know the interactions between the propulsion subsystem and the spacecraft. One possible interaction between the plume and the spacecraft surfaces is erosion of the surfaces from impinging plume particles. Erosion rates can be monitored through the use of witness plates. These samples are placed in a variety of locations about the thruster in order to detect plume-induced erosion. However, not much public data of this type exists, and thus, engineers are left to conduct extensive testing in order to mitigate the risks associated with using the thruster near surfaces such as solar arrays.

Because of the new-found interest in Hall thrusters, satellite designers are demanding detailed understanding of the thruster's operation and interaction with the spacecraft. It is difficult, however, to predict those interactions without thorough experimental data. Consequently, two- and three-dimensional models have been developed to study the physics of Hall thrusters and to simulate the interaction phenomenon between the spacecraft and the thruster plume.

1.1 Previous Modeling Research

1.1.1 Acceleration Channel Modeling

In 1993, Lentz developed a quasi-one-dimensional model of the acceleration channel of a Hall thruster [13]. The model predicted plasma quantities and thruster performance along the length of the channel in order to understand the acceleration process in the channel. Experimental data from a Japanese Hall thruster was used to validate the model, and it was shown that the model matched the experimental data quite well. This accuracy represented a significant improvement over previous 1D models.

The success enjoyed by the 1D model prompted the development of a two-dimensional model by Fife in 1995 [9]. The code incorporated the 1D model and extended it in the radial direction in the channel. Instead of designing the model around the Japanese thruster, the model used thruster geometry as an input and thus can theoretically be operated using any thruster geometry. The model was validated against performance data for an SPT-100.

Since 1995, the model has undergone extensive revision in order to improve its accuracy [10]. In particular, low-frequency discharge oscillations and wall interactions have been examined. Currently, research is being conducted to generalize the two-dimensional model for a variety of thruster geometries [24] including the SPT-70 [10]. Double ionization within the accelerator chamber is also being investigated.

1.1.2 Plume Modeling

Both an axisymmetric two-dimensional model and a three-dimensional computational model for a plasma plume were developed by Dr. David Oh at MIT in 1996 [16]. The models utilize a computational scheme which combines Particle-in-Cell (PIC) and Direct Simulation Monte Carlo (DSMC) methods to address the physics of expanding plasma plumes and plume interactions with spacecraft. Large-scale plume structures with realistic thruster geometries, as well as erosion of surface materials such as silver, quartz, and silicon, can be accurately simulated. The result is the first-ever use of such a PIC-DSMC scheme in any application and the first comprehensive numerical model of a Hall thruster plume.

1.2 Objective of this Research

The research poses the question: can a complete computational model of a Hall thruster be generated from the two existing models which have been developed at MIT over the past few years? This thesis presents the key integration issues facing the generation of a complete computational model of a Hall thruster and details the modifications to the existing codes necessary for integration. The model would combine a hybrid Particle-in-Cell (PIC) method for the thruster acceleration channel with a combination Particle-in-Cell (PIC)/Direct Simulation Monte Carlo (DSMC) method to simulate collisions in the plume. Improvements have been made to the plume model, including the addition of the surface sputtering yield dependence on angle of incidence and the development of an improved source model. The resulting integrated model would run on a UNIX workstation and would be valuable to designers interested in evaluating the impact of an SPT on realistic satellite configurations.

Chapter 2 presents the fundamental theory behind Hall thrusters and discusses the computational methods to be employed in the combined model. Chapter 3 delves into a detailed discussion of the primary issues which must be addressed before the complete model can be implemented and outlines the techniques used in the plume code source model sensitivity analysis. Results are presented in Chapter 4 with an analysis of the enhancements to the plume model. Finally, Chapter 5 concludes with a summary of the work and provides an outline for generating the complete computational model of a Hall thruster.

Chapter 2

Fundamental Theory

2.1 Hall Thruster Operation

A Hall thruster is an electric propulsion device in which ions are electrostatically accelerated in the thrust direction. A magnetic field is established in the radial direction in the acceleration channel. It is important to note that the length of the acceleration channel must be much smaller than the ion Larmor radius, so that ions can accelerate across the exit without being affected by the magnetic field. Electrons are emitted by the cathode which are attracted to the anode and enter the channel. The electrons, whose Larmor radius is much smaller than that of the ions, are trapped by the radial magnetic field. These electrons serve to ionize the xenon gas which flows into the channel. The ensuing ions are then accelerated by the axial electric field across the exit of the thruster. The magnetic pressure from the electrons which are trapped at the exit by $\vec{E}\times\vec{B}$ drift gives rise to the thrust force on the structure. Figure 2-1 shows a schematic for this process.

A typical Hall thruster is given in Figure 2-2. The SPT-100 is one type of Hall thruster and is used as the baseline configuration in the following analyses. Nominal operating conditions of the SPT-100 are assumed in the analyses and are summarized in Table 2.1.

Anode Mass Flow Rate	4.99 mg/s
Cathode Mass Flow Rate	0.38 mg/s
Specific Impulse	1610 s
Thrust	84.9 mN
Power	1350 W
Efficiency	49.7 %
Discharge Voltage	300 V
Discharge Current	4.5 A
Inner Anode Radius	28 mm
Outer Anode Radius	50 mm
Double Ionization Fraction	20%
Axial Ion Velocity	17020 m/s
Axial Ion Temperature	~3 eV

Table 2.1: SPT-100 Nominal Operating Conditions [16]

2.2 Computational Schemes

The plume computational model primarily used in this research was written by Dr. David Y. Oh, a former Space Systems Laboratory (SSL) research assistant [16]. In addition, results from the engine code written by J. Michael Fife, also an SSL research assistant, are used in the analysis [10]. The theory presented in this chapter draws heavily from their work.

2.2.1 Particle-In-Cell

Particle-in-Cell (PIC) methods are commonly used in determining plasma behavior over time. It is computationally expensive to track particles which number on the order of 10^{20} and calculate their properties at each time step. PIC codes eliminate the need to track individual particles by examining the collective behavior of the plasma.

In the PIC method, macroparticles with the correct charge to mass ratio are used to represent a larger set of particles. These particles are weighted to a grid and the local charge density in each grid cell is found. The local electric field is then determined by first solving Poisson's equation[1],

$$\nabla^2\phi = \frac{-\rho}{\epsilon_o} \tag{2.1}$$

where ϕ is the potential and ρ is the charge density, and then differentiating the potential.

$$\vec{E} = -\vec{\nabla}\phi \tag{2.2}$$

The electrostatic force is then interpolated at each particle position, and the particles are moved by solving the electrostatic equations of motion at each point.

$$\frac{d\vec{r}}{dt} = \frac{q\vec{E}}{m} \tag{2.3}$$

A finite difference method, such as the leapfrog method [4], is used to perform the integration of the equations of motion.

The PIC method is valid in regions of relatively dilute plasmas. This method is statistically accurate for no fewer than 10 particles per cell.

2.2.2 Direct Simulation Monte Carlo

PIC codes are used to describe collisionless plasmas. In order to simulate collisions, albeit rare occurrences, Monte Carlo schemes must be used. The Direct Simulation Monte Carlo (DSMC) method models short-range collisions. Self-consistent electric fields are not, however, considered in the formulation of the technique. DSMC alone cannot be used to model charged particles if the particles' motion affects the fields.

Like PIC, DSMC uses macroparticles to simulate a larger set of particles and is time-accurate. In the implementation of the collision routine, a local time counter is assigned to each grid cell and compared against a global time counter. If the local time is less than the global time, a collision is executed. An appropriate collision pair

---

[1] Note that for most problems in electric propulsion, Poisson's equation cannot be used due to strong quasi-neutrality in which $\rho = 0$. Computations are unstable unless the cell size is smaller than the Debye length. The potential is instead adjusted such that the divergence of the current is zero.

is randomly chosen within the cell, and the pair's individual velocities are modified. The local time counter is incremented by the inverse of the collision frequency for the two particles. This routine is executed cell by cell for each iteration. The method is statistically accurate for no fewer than 20 macroparticles per cell.

2.2.3 Acceleration Channel Model

A "hybrid-PIC" formulation is used in the acceleration channel model. As opposed to a standard PIC scheme in which both ions and electrons are simulated, the acceleration channel model simulates only heavy species, ions and neutrals. Electron motion is described by integrating the fluid equations of motion. This is why the method is called "hybrid."

The local potential is not calculated using Poisson's equation. Instead, a quasineutrality assumption is made which allows the Boltzmann equilibrium equation to be used to generate the potential. Please see additional discussion in Section 2.2.4.

Several other modifications were made to the standard PIC method. These include the adaptation of the method to a non-uniform grid and the use of variable macroparticle weights.

Convergence is achieved when fluctuations in the code reach a regular frequency and amplitude or when the averages of the output parameters reach a constant. The time step used in this method is $5 \cdot 10^{-8}$ s ($8 \cdot 10^{-9}$ s/rad).

2.2.4 Plume Model

The plume code utilizes a combination PIC-DSMC algorithm to track plasma behavior while including collisions. The basic PIC algorithm is the same, except instead of solving Poisson's equation for the electric field, a simplified, equilibrium form of the electron momentum equation is used. The DSMC routine is incorporated into the PIC algorithm which modifies the particles' trajectories as collisions occur.

For a Hall thruster plume, the electron momentum equation reduces to

$$n_e q\vec{E} - \vec{\nabla} p_e = 0 \tag{2.4}$$

where n_e is the electron number density and p_e is the electron pressure, if all scattering and magnetic effects are neglected. Assuming an isothermal plume, this can be written as

$$n_e = n_o e^{\frac{-e\phi}{kT_e}} \tag{2.5}$$

in which T_e is the electron temperature. This result is simply Boltzmann's equilibrium law. The reduction to this form relieves some of the computational cost associated with iteratively solving for the potential by using the Poisson equation. In fact, the Poisson equation can longer be used to calculate the potential, since the formulation assumes a priori that the plasma is quasi-neutral. The local plasma potential can be determined by simply inverting the Boltzmann equation at each node.

The collisions which are modeled include neutral–single ion charge exchange, neutral–double ion charge exchange, and neutral–neutral, neutral–single ion, and neutral–double ion elastic collisions. The charge exchange collisions are the dominant interactions. Each collision has its own characteristic frequency, thus the local time counters within each cell are dependent upon the collision time scales. A multi-species time counter is employed which averages the individual time counters for each type of collision and is given by

$$\Delta t = \frac{W_L V}{N_o W_o (2N_1 W_1 + 2N_2 W_2 + \frac{N_o W_o}{2})(\sigma c_r)_{ij}} \tag{2.6}$$

where W is the macroparticle weighting factor, V is the volume of the cell, N is the number of macroparticles in each cell, σ is the collision cross section, and c_r is the relative speed of the collision pair. σ and c_r are evaluated for the particular type of collision which occurs and are used in the calculation of the local time step. The subscripts of 0, 1, and 2 correspond to neutrals, single ions, and double ions, respectively. Note that the ij subscript notation does not correspond to the summation over collision pairs but to the cross section and relative speed of the considered collision pair.

The collision cross sections of for the various processes are given in Table 2.2.

Collision	Cross Section Relation
$Xe - Xe^{+}$ CEX	$\sigma_{CEX} = (-0.88 ln c_r + 15.13)^2 \cdot 10^{-20}$ m^2
$Xe - Xe^{++}$ CEX	$\sigma_{CEX} = (3.41 \cdot 10^{-9} - 2.70 \cdot 10^{-10} ln c_r)^2$ m^2
$Xe - Xe$ Elastic	$\sigma_E = (2.12 \cdot 10^{-18} c_r^{-0.24})$ m^2
$Xe - Xe^{+}$ Elastic	$\sigma_E = (\frac{8.28 \cdot 10^{-16}}{c_r})$ m^2
$Xe - Xe^{++}$ Elastic	$\sigma_E = 2(\frac{8.28 \cdot 10^{-16}}{c_r})$ m^2

Table 2.2: Collision cross sections for collisions considered in the plume model. [16]

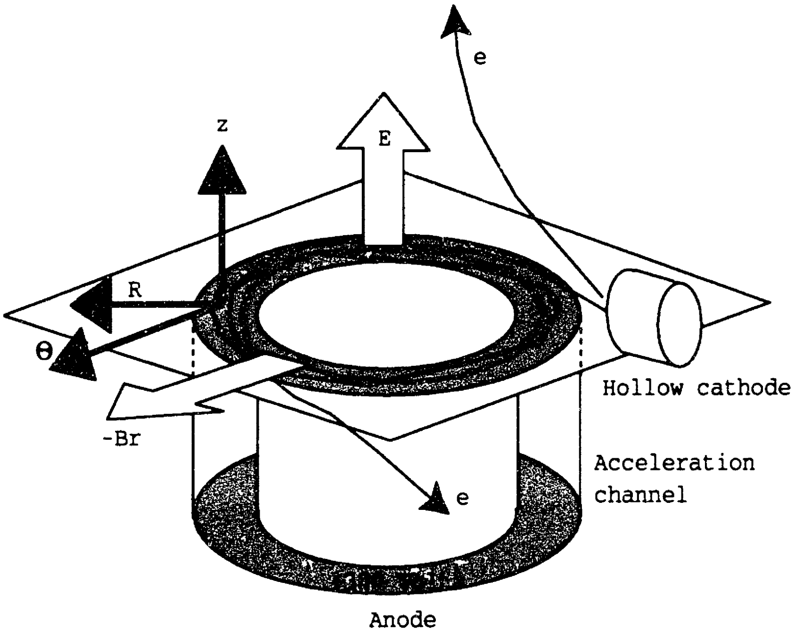

Figure 2-1: Hall thruster operation.

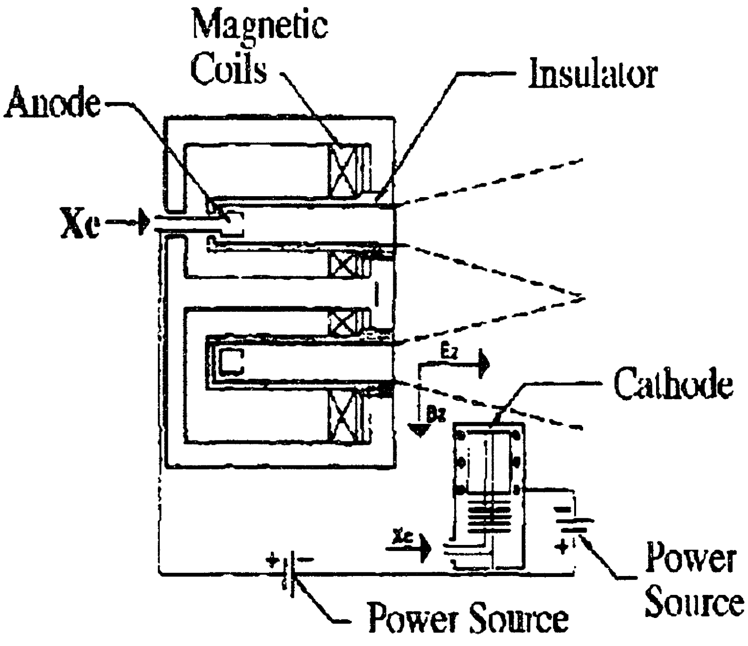

Figure 2-2: Schematic of a typical Hall thruster.

Chapter 3

Integration Issues

Integration of the interior and exterior Hall thruster computational models is scheduled to occur over the next few years. This work is the beginning of the integration process. This chapter outlines and explores a number of the salient integration issues and describes the methodology by which these issues were addressed in the Results chapter.

3.1 Physics Issues

3.1.1 Source Model

Plasma Oscillations

In both experimental and numerical results, plasma oscillations have been observed. The most prominent mode is at approximately 30 kHz.

Plasma oscillations are of concern for spacecraft-plume interactions. It is believed that an increase in the oscillations produces an increase the radiated electromagnetic interference (EMI) from the plasma. Oscillations can also cause a phase shift in a communications signal which passes through the plume. [21]

It has been proposed that the instability arises from an ionization interaction between ions and neutrals [11]. An analysis of ion and neutral dynamics was conducted, and it was concluded that the resulting frequency matched that of the low-frequency discharge oscillations observed. The frequency was found to be a function of the length of the ionization region and the velocities of the ions and neutrals across that region. However, new experimental results appear to contradict this theory, in the sense that the ion-acoustic modes of the cavity seem to determine the oscillation frequency [10].

Dr. Oh, however, did not take this effect into account in the development of the plume model. His results are based upon a steady source which introduces new particles at the exit plane at the beginning of every iteration.

If EMI concerns and communications concerns are to be properly addressed by the end-to-end model, plasma oscillations must be incorporated into the plume model. The first issue is the resolution of the plume model: is the plume simulation robust enough to model the low-frequency discharge oscillations? If not, the question arises whether or not it is useful to address the oscillations.

Ionization

Currently, the acceleration channel model does not include the effects of double ionization. Doubly-ionized xenon particles have been measured to constitute up to 20% of the particles in the plume [14]. The double ion fraction, however, can be post-calculated using values for electron and neutral densities and electron temperature [24].

Assuming stationary neutrals and ions relative to electrons and considering a Maxwellian distribution of electrons, the local production rate of ions is described by

$$\dot{n}_{Xe^{++}} = n_n n_e \frac{8\pi}{{m_e}^2} \int \epsilon \sigma_{Xe^{++}}(\epsilon) f_M(\epsilon) d\epsilon \tag{3.1}$$

where n_n is the neutral density, n_e is the electron density, m_e is the electron mass, ϵ is the energy variable, σ is the collision cross section for doubly-charged ions, and f_M is the Maxwellian distribution in energy [15]. The total production rate of double ions can then be found by integrating the local production rate over the domain.

Post-calculations of the double ion production rate suggest that only a few percent of the xenon neutrals are ionized versus the experimental values between 10% and 20% [21]. To check the validity of this calculation, enhancements to the engine code are currently underway which will incorporate double ions into the model.

In the meantime, the sensitivity of the plume code to double ion inclusion can be explored. The change in plume model output without xenon double ions can be gauged by changing the double ion fraction at the anode in the plume input file. Thus, the importance of the double ions in the model accuracy can be determined.

Exit Plane Distribution

The region of importance for the integration is the exit plane of the thruster model. Results at this location will serve as input to the plume simulation. Thus, accuracy in this region is vital.

In addition, the plume code's source model is of key importance in the integration of the thruster acceleration chamber and plume models, since the source is the sole interface between the hybrid-PIC and the PIC-DSMC codes. Thus, output from the hybrid-PIC model must be compatible with the plume code for a complete simulation to operate accurately.

The experimental ion flux and simulated ion flux are shown in Figures 3-1 and 3-2. The experimental data were taken from what appears to be akin to an SPT-70, not an SPT-100. However, as will be explained below, the plume model uses the data as input for the SPT-100. The simulated data are based on the SPT-100 where the inner channel radius is 34.4 mm and the outer channel radius is 50 mm. However, results from the two, such as ion current density as a function of radius, are difficult to compare without normalization to a standard channel width.

As alluded to above, the plume simulation begins at the thruster exit plane. A source model consisting of ion current density and beam divergence angle distributions was constructed to reflect experimental data taken near the exit plane of an SPT. Beam divergence angle is defined as the angle formed from the components of the ion flux vector as measured from the centerline of the annular thruster exit.

The source model, however, is based upon only one set of empirical data for ion current density and beam divergence angle near the thruster exit plane. Thus, the code has not been extensively tested with a variety of source model inputs. The data for the existing source model are also suspect: no error bars are present in the data, and the asymmetric shape of the ion current density distribution suggests that the thruster has seen some damage or wear.

A second source model was created from the output of the hybrid-PIC code to quantify the sensitivity of the plume code to variations in source input and to gauge the compatibility of the interior and exterior thruster models. The source model is comprised of a current probability distribution function and a beam divergence angle distribution function. The probability distribution function gives the probability an ion will cross the exit plane at a radial distance less than a given location, r, while the beam divergence function provides the mean angle measured from the thruster centerline at which an ion crosses the thruster exit. Tests were run using the different combinations of distribution and beam divergence functions in the plume model to measure the impact of the source on the model results.

The probability distribution function is calculated by dividing the current through an annular area from the inner channel radius to a distance r by the total current at the thruster exit. Using a distribution for ion current density, one can express the differential current expected through an annular area as

$$dI = e\Gamma_z(r) \cdot dA_{flux} = 2\pi r j_z(r) dr, \tag{3.2}$$

where Γ_z is the axial ion flux through the thruster exit as a function of radius, and dA_{flux} is the differential flux area. The above equation is then integrated from the inner radius of the channel to a distance r to obtain the current. The total current through the exit is given by the integral of the ion current density times the flux area from the inner radius to the outer radius of the channel. Thus,

$$P(r) = \frac{\int_{r_i}^{r} 2\pi r j_z(r) dr}{\int_{r_i}^{r_o} 2\pi r j_z(r) dr}, \tag{3.3}$$

where r_i is the inner channel radius and r_o is the outer channel radius.

Ion Energy

A secondary issue regarding the source model concerns the axial ion temperature at the thruster exit plane. Although the assumptions upon which the original plume code results were based allow the accurate simulation of macroscopic properties of the plume, inconsistencies appear between the energy results produced by the code and experimental data due to an incorrect choice of axial ion temperature at the exit plane.

Figure 3-3 and 3-4 show the experimental Retarding Analyzer Potential (RPA) data and simulated results. RPA data taken in an arc 60 cm away from the thruster exit indicate that there is a similar energy distribution of particles at a variety of angles away from the thruster centerline. The model, however, predicts a distribution in which the energy curve's peak shifts towards decreasing energy as the angle increases away from the centerline. This shift in the peak of the ion energy can be readily seen in Figure 3-4. Corrections to the axial ion temperature assumed in the source model have explained this behavior and have allowed the matching of the simulation with experiment. A discussion follows in Section 4.1.2.

3.1.2 Sputtering Model

While designing the components of a satellite system, engineers must know the interactions between those components. Thus, the interaction of the thruster plume with the surfaces of a spacecraft is a critical issue in satellite design. These interactions can include, but are not limited to, surface charging, deposition and contamination, erosion, communications interference, and thermal interactions with the spacecraft. Through the development of a surface interaction model, the three-dimensional PIC-DSMC plume model has the ability to predict erosion on spacecraft surfaces.

Incident particles on solid surfaces can undergo backscattering, come to thermal equilibrium and evaporate at the surface, provoke secondary electron emission, remove atoms from the surface (sputtering), or cause radiation damage [8]. For high-mass particle bombardment at low energies, sputtering is the dominant effect [3]. Since, the

SPT plume ions have been shown to have energies between 100 and 400 eV, surface sputtering must be considered.

In the three-dimensional model, any particle crossing an object boundary is removed or reflected as appropriate for that species. Ions are neutralized and removed from the simulation, while neutrals are reflected back into the domain in a manner consistent with an ideal specular surface.

Oh calculated sputtering rates by tabulating the material removed by each particle striking the simulated surfaces of the spacecraft. The amount of material lost was determined by multiplying an energy-dependent sputtering coefficient by the macroparticle weighting factor. A particle's impact energy was given by the sum of its kinetic energy and the energy gained or lost in the sheath. Neutrals were assumed to undergo no acceleration in the sheath region.

The surface model has the ability to predict erosion rates for silver, silicon, and quartz: materials which are commonly used for solar array surfaces and interconnectors. Each material's erosion rate was calculated using a linear relation between sputtering yield of normally incident particles and particle impact energy:

$$S = AE + B \tag{3.4}$$

where S is the sputtering yield in m^3/atom and E is the energy in eV. The fit coefficients, A and B, are given in Table 3.1.

Material	*A*	*B*
Silver	$1.25 \cdot 10^{-31}$	$-5.034 \cdot 10^{-30}$
Silicon	$2.12 \cdot 10^{-32}$	$-2.43 \cdot 10^{-30}$
Quartz	$2.80 \cdot 10^{-32}$	$-7.15 \cdot 10^{-31}$

Table 3.1: Fits for sputtering yield of normally incident particles, Equation 3.4, for silver, silicon, and quartz. [20]

The sputtering yield, however, is not simply a function of impact energy alone. It has been observed that atoms striking at non-normal angles to the surface may have higher sputtering coefficients than those striking normal to the surface [2]. Thus, the original interaction model tended to under predict the erosion rate. The inclusion of this angular dependence represents a significant enhancement over the original sputtering model.

Figure 3-5 shows the sputtering yield versus angle of incidence for particles with energies in the keV range. The sputtering yield for xenon into molybdenum increases over the normal yield by as much as a factor of six at angles between 70° and 80° from the normal. As a first-cut approximation, the data can be incorporated in the surface interaction model by multiplying the normal sputtering yield used in the model by the ratio of the yield dependent upon impact angle to the normal yield given in Figure 3-5. The order of magnitude effect of the angular dependence on surface erosion can then be gauged.

The data were taken at only one incident particle energy level: 30 keV. Since little information is available for sputtering at lower energies, an upper limit to the sputtering can be established based upon high-energy sputtering data. Experimental data for xenon ions sputtering silver, copper, molybdenum, and silicon targets have suggested that increasing incident energy increases the sputtering yield for energies up to approximately 100 keV [2]. Also, although the angular dependence for xenon sputtering silver is unknown, the angular dependence was assumed to be comparable to that from xenon sputtering other materials for this first-cut angular dependence analysis.

The regime, however, in which the xenon ions, double ions, and neutrals of the plume model lie is between 0 and 400 eV. Thus, the low-energy sputtering information becomes vitally important to predict erosion on the spacecraft surfaces accurately.

A second set of sputtering data was adapted from an empirical model developed by Yamamura, et. al, [25] in 1983 and can be used for low-energy, heavy-ion sputtering. This model takes into account the effects of energy dependence in the sputtering at non-normal angles of incidence as well as the effects of material dependence.

The correction to the normal sputtering yield rate is given by

$$\frac{Y(\theta)}{Y(0)} = \cos^{-f}\theta e^{-\Sigma(\cos^{-1}\theta-1)} \tag{3.5}$$

where θ is the angle of incidence as measured from the surface normal and f and Σ are adjustable, energy-dependent, best-fit parameters to experimental data given by

$$f = f_s[1 + 2.5\frac{(\frac{E_{th}}{E})^{\frac{1}{2}}}{1 - (\frac{E_{th}}{E})^{\frac{1}{2}}}], \tag{3.6}$$

$$\Sigma = f\cos(\theta_{opt}) = f\cos(90^o - 286\psi^{0.45}); \psi \propto \frac{1}{\sqrt{E}}. \tag{3.7}$$

f_s is taken from an earlier work by Sigmund [22], and E_{th} is the threshold energy: the minimum energy required for sputtering to occur. Thus, the Yamamura formula takes into account both the incident energy and angle in the correction to the normal yield rate.

The Yamamura model, with average best-fit parameters as given above, reasonably approximates experimental data over a wide range of angle of incidence. Figures 3-6, 3-7, and 3-8 show how the Yamamura model fares against empirical data for xenon ions into copper. The solid line gives the experimental data curve fit, while the bolder line marked with crosses gives the Yamamura model. The model appears to best predict the data in the few keV range. Therefore, from viewing the figures, we should expect below this range, the sputtering is under predicted, while over this range, the sputtering is over predicted.

3.1.3 Sensitivity Analysis

The sensitivity of the plume model to the source is measured as the response of the erosion rate to various source parameters. Since designers are concerned with the plume-induced erosion effects of spacecraft surfaces, the erosion rate becomes a logical choice for the systematic quantification of sensitivity to the source model. Different sources vary in the angle at which the ions exit the thruster as well as in the ion distribution at the exit plane. Consequently, that variation yields variability in erosion rates.

Thus, erosion rate is used as the metric to quantify the plume model sensitivity to the source. For sets of rough data, a multivariate polynomial fit using a least squares approximation can be used to describe the sensitivity. For example, the erosion as a function of two source parameters, x and y, can be described by the bivariate polynomial

$$g(x,y) = ax^2 + by^2 + cxy + dx + ey + f \tag{3.8}$$

where a through f are coefficients to be fitted.

Quite a number of source parameters can be considered for the sensitivity survey. Also, within some parameters, such as the ion current density distribution, others may be obtained. Since the ion current density itself is a third order polynomial with four coefficients, at least 15 data points must exist to generate a second-order polynomial statistical fit for the sensitivity to the ion current density distribution. Each data point corresponds to a run of the code; thus, this process quickly becomes time-intensive. Hence, we have chosen to focus on collective models before distinguishing between individual parameters.

The domain of analysis for the sensitivity is shown in Figure 3-9. The domain consists of two axes: that containing the source model and that containing the sputtering model. The origin represents the baseline case; here, the source model is that generated from the Russian SPT data for the ion current density and beam divergence angle, and the sputtering model does not include the correction for the dependence upon impact angle. The bounds of the domain consist of the source model generated by the engine code and the Yamamura model to capture angular dependence of surface sputtering.

As a first-cut analysis, we have concentrated on describing the bounds to the sensitivity analysis and chosen the ion current density and beam divergence angle distributions as the only parameters to vary. The interactions within the domain as well as the sensitivity to other source parameters will be explored in future work [18].

3.2 Computer Science Issues

3.2.1 Automatic Source Model Generation

A short-term solution to integration is an automatic source model generation program for the plume code. The interior model's output can be sampled to reconstruct the ion current density and beam divergence angle distributions at the exit plane. The source file for the plume code can then be modified to include the new distributions.

The grid (grid.dat) and the ion flux (flux_i.dat) data files are created as the interior model runs. The grid is read directly into a data structure and stored in order to map the ion current density and beam divergence angle to locations in the $z - r$ plane. The ion current density is calculated at each node from the ion flux by

$$\vec{\Gamma} = \vec{j}/e \tag{3.9}$$

in which $\vec{\Gamma}$ is the ion flux, $\vec{j}$ is the ion current density, and e is the electron charge. Since the flux vector is broken down into its (z, r) components in the output file, the beam divergence angle can also calculated from the flux data. The beam angle is measured from the thruster's centerline of the annular region.

A least squares fit is then performed on the data, since they are most readily described by a polynomial. Thus, a standard least squares fit is used from Numerical Recipes [17]. Other fits may be used as proven necessary. Currently, the ion current density distribution is described by a third order polynomial, while the beam divergence angle distribution is fitted to a fourth order polynomial.

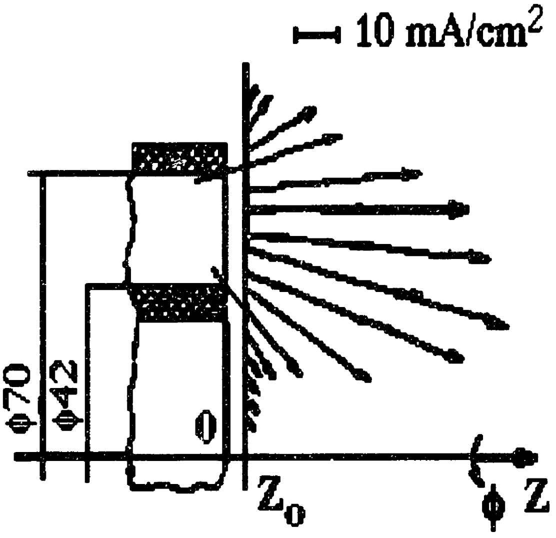

Figure 3-1: Current density measured 4 mm from thruster exit. [12]

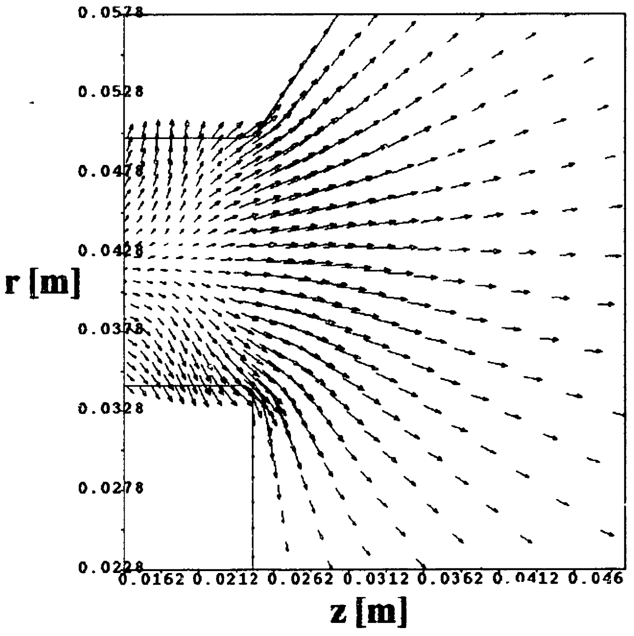

Figure 3-2: Simulated ion flux at thruster exit.

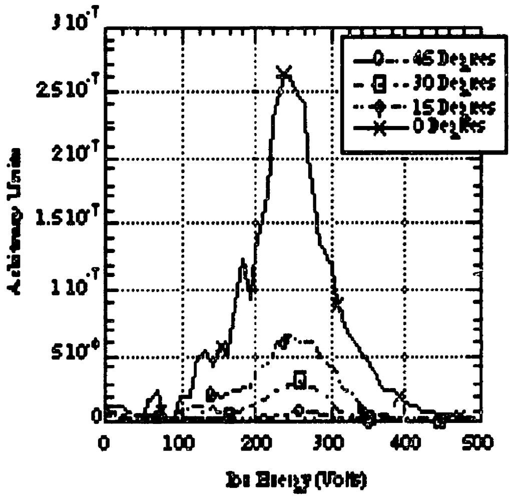

Figure 3-3: RPA energy distribution taken 50 cm from thruster exit. [Marrese/Gallimore] $P = 5.2 \times 10^{-5}$ Torr

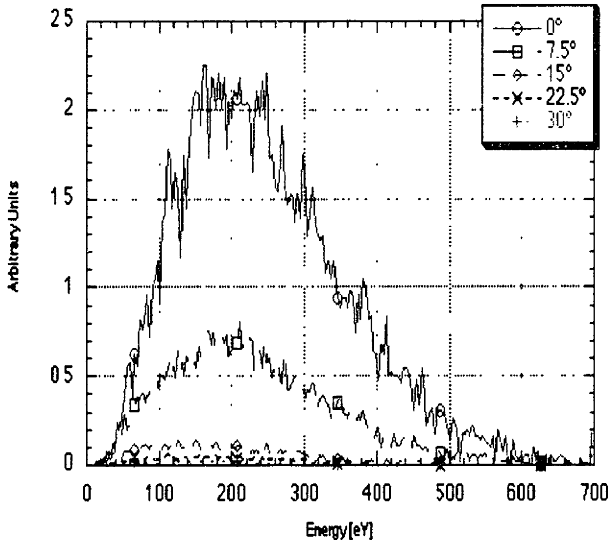

Figure 3-4: Simulated RPA energy distribution taken 60 cm from thruster exit. $T_i = 34.0$ eV, $P = 2.2 \times 10^{-6}$ Torr

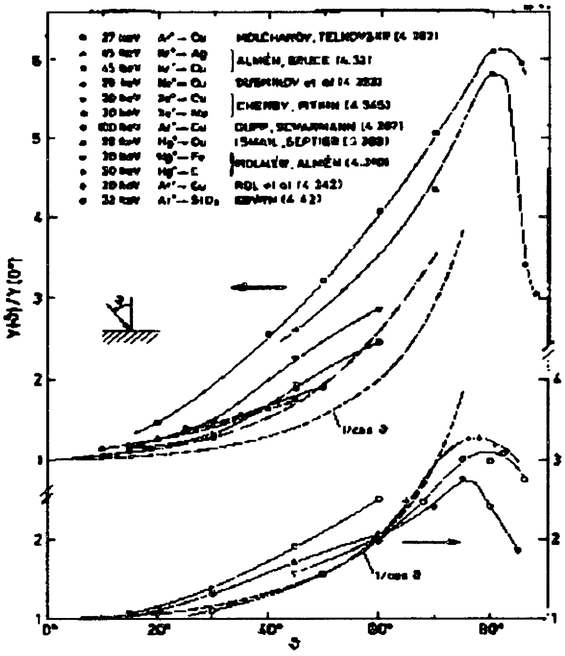

Figure 3-5: Sputtering yields in keV region as a function of angle of incidence [2].

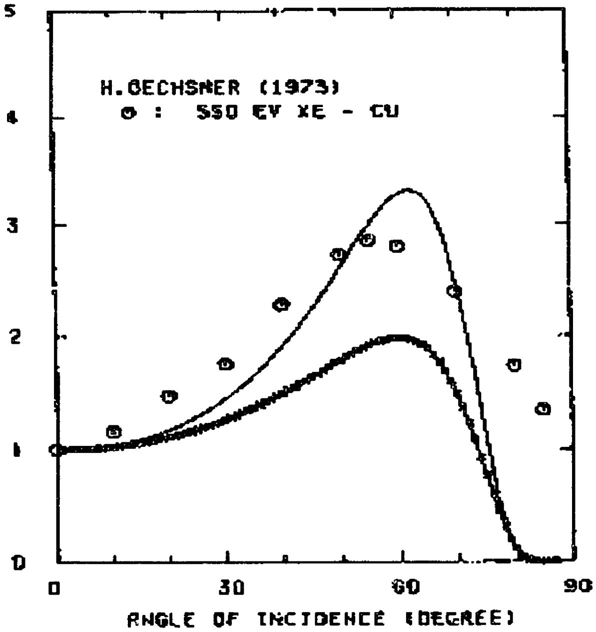

Figure 3-6: Sputtering yield for $Xe^{+} \rightarrow Cu$ at 550 eV as a function of angle of incidence [25].

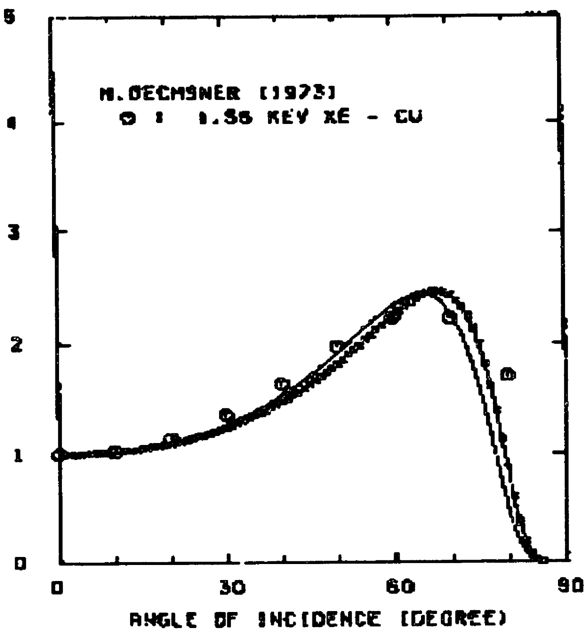

Figure 3-7: Sputtering yield for $Xe^{+} \rightarrow Cu$ at 1.55 keV as a function of angle of incidence [25].

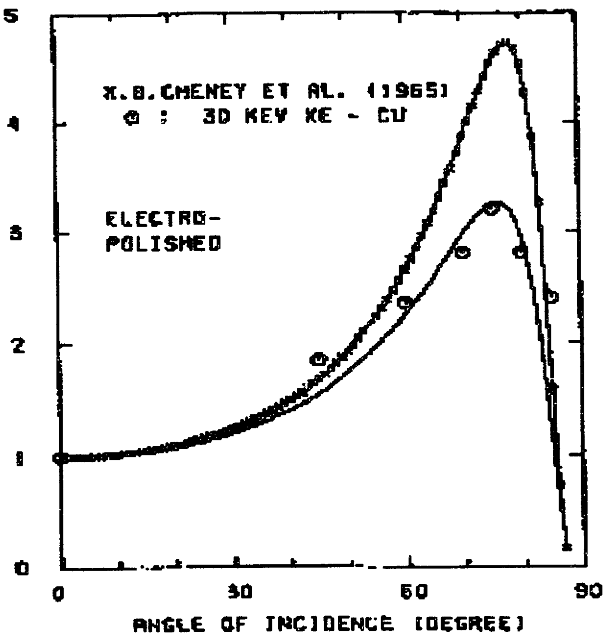

Figure 3-8: Sputtering yield for $Xe^{+} \rightarrow Cu$ at 30 keV as a function of angle of incidence [25].

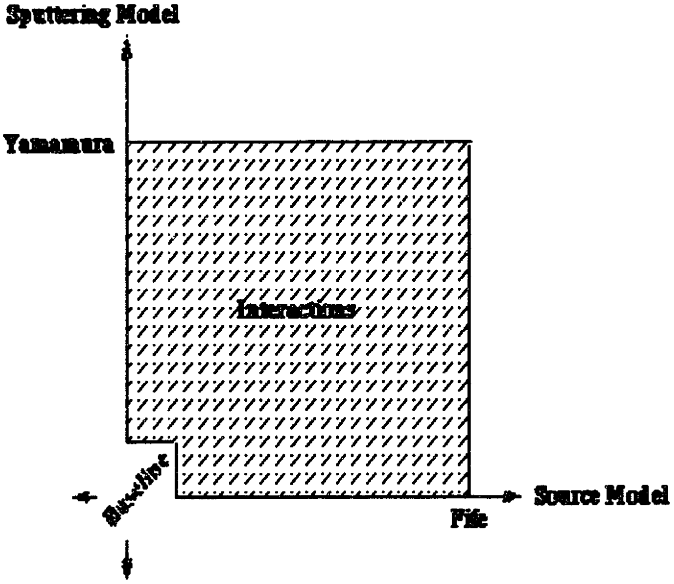

Figure 3-9: Domain of analysis for sensitivity calculations. Note: baseline source and sputtering models lie at the origin.

Chapter 4

Results and Discussion

4.1 Source Model

Unless otherwise specified, the SPT-100 operating conditions are given in Table 2.1.

4.1.1 Plasma Oscillations

Hall thruster plasma oscillations having a frequency of 30 kHz have been measured and can be simulated using the hybrid-PIC engine code. However, the plume model does not currently take the oscillatory behavior of the plasma properties into account when infusing new particles into the simulation. For plasma oscillations to be addressed, the plume model must have the ability to resolve these low-frequency discharge oscillations.

As discussed in Section 2.2.2, the plume model keeps a global time counter whose time step is 0.1 in normalized units. Time was normalized to the plasma ion frequency, ω_{pi}, and thus, the time increment for every iteration is

$$\Delta t_g = \frac{0.1}{\omega_{pi}} \approx 8.67 \cdot 10^{-7} s/rad. \tag{4.1}$$

The period of the oscillation is

$$t_{osc} = \frac{1}{2\pi \cdot 30000} s/rad \approx 5.3 \cdot 10^{-6} s/rad. \tag{4.2}$$

Therefore, at each time step,

$$\frac{\Delta t_g}{t_{osc}} \approx 0.16 \tag{4.3}$$

oscillations are seen. That is, six iterations are needed to go through one period of the oscillation. Since the plume code samples after every ten iterations, the sampling sees approximately the same values of the plasma properties if the sampling begins at the mean values. If sampling does not begin at the mean values, the sampled plasma properties would alternate in value. Thus, the plume model does not adequately resolve the oscillations.

If the Δt_g were one-tenth of its value now, 60 iterations would be performed per cycle. Although this seems to be adequate, the total number of steps for the generation of good statistics from the plume code increases by a factor of ten. 10,000 iterations are necessary to generate good statistics for erosion data; thus, the total time to generate the statistics is Δt_g times 10,000. Conserving the total time and decreasing Δt_g by a factor of ten results in ten times the number of iterations. 10,000 iterations takes approximately four hours to run on an SGI Octane with a 175 MHz R10000 processor. Hence, the total computational time necessary becomes 40 hours.

A test can be devised to measure the effect of the oscillations on the plume structure. A periodic source can be incorporated into the plume model such that at each iteration, particles with a new set of properties are injected into the simulation. The time step can also be decreased in order to better resolve the oscillations.

A further discussion detailing the implications of changing the plume model to resolve oscillations will be proffered in future work [18], including an examination of the number of particles per cell necessary for adequate oscillation resolution.

4.1.2 Ion Energy

In order to validate the three-dimensional plume model, results from the simulation were compared against experimental plume data [16]. Although the model results agreed well with plume ion current density data taken by Marrese and Gallimore at the University of Michigan (1996) and Manzella at NASA Lewis (1995), simultaneous matching of the ion energy distribution data and the ion current density data could not be achieved.

In particular, the experimental data suggests that the peak location in the energy distribution is invariant with the angle from the centerline, as shown in Figures 4-1 and 4-2. This behavior had not been seen in the simulations.

Figure 4-3 shows the simulated Retarding Potential Analyzer (RPA) distribution at a chamber pressure of 2.2×10^{-6} Torr, taken in a 60-cm arc away from the anode. This corresponds to the conditions under which Manzella operated. The axial ion temperature at the exit was assumed to be 34.0 eV. Here, the peak of the energy distribution shifts toward lower energies as the sample angle increases. This indicates that the particles reaching those angles (as measured from the thruster centerline) in the plume do not carry the same energy distribution as those closer to the centerline.

Another difference between the simulated data at varying axial ion temperatures is the presence of a high energy tail in Figure 4-3. Ions exist which have energies of up to 600 or 700 eV. As a result, the plume shape and erosion rates seen would have a different character.

Assumptions regarding the plasma axial ion temperature in source model have been identified as the main contributors to these disparities.

Oh had initially assumed an axial ion temperature of 34 eV, since he felt it gave better agreement with the observed structure of the experimental ion current density data [16]. This decision was apparently supported by the shape of the experimental energy distributions in the RPA data of Figures 4-1 and 4-2 which show half-widths in the 50 eV range. However, the shape of these distributions can be misleading.

If we treat the RPA data as a Gaussian distribution, the energy distribution can be written as

$$f(\epsilon) \propto e^{-\left(\frac{\sqrt{\epsilon}-\sqrt{E_d}}{\sqrt{T}}\right)^2} \tag{4.4}$$

where E_d is the drift energy and T is the ion temperature. The temperature can be calculated by finding the energy at which the energy distribution is equal to

$$f(\epsilon) = Peak\_Height * e^{-1}. \tag{4.5}$$

The corresponding energies can then be placed into the condition

$$T = (\sqrt{\epsilon} - \sqrt{E_d})^2, \tag{4.6}$$

and the equation can then be solved for temperature. Using the data in Figures 4-1 and 4-2, the temperatures were calculated to be in the range from approximately 0.6 eV to 4.5 eV.

This is supported by the laser-induced fluorescence data of Manzella that suggested an ion temperature around 3.4 eV. Figure 4-4 shows the simulated RPA distribution using the same conditions as before but with a corrected axial ion temperature of 3.4 eV, an order of magnitude lower than had been previously assumed.

The differences between Figures 4-3 and 4-4 are obvious. Changes in the axial ion temperature produce significant changes in the ion energy distribution in the plume. Specifically, Figure 4-4 does not show the shift in the peak of the distribution with angle, matching the experimental behavior. Furthermore, the high energy tail is now absent.

When compared with experimental RPA data given in Figures 4-1 and 4-2, the simulated RPA distribution with the best correlation is the distribution measured using an axial ion temperature on the order of a few eV's. Although the operating voltages used in the experimental data are higher than what is given by the simulation, what is of concern here is the shape of the RPA distribution rather than the exact temperature.

The physical explanation for the difference between Figures 4-3 and 4-4 is that the high ion temperature allows the thermal velocity of the ions to be much greater than empirical data. The added energy channels most of the ions around the centerline, while the lower energy ions are turned outward by the electric field. Consequently, ions with lower energies will be found at angles away from the centerline.

Decreasing the source ion thermal energy, however, causes the ion energy distribution to be similar at all angles. All ions have the same probability of reaching a given sampling location, because the ion thermal velocity in each direction is of the same order.

The assumption of 34.0 eV ion temperature is clearly inadequate. An axial ion temperature on the order of a few eV's must be selected before full validation can be achieved.

4.1.3 Ionization

The sensitivity of the plume output to double ionization was measured by comparing a run which considered a double ionization fraction of 20% with a run which did not include doubly-ionized xenon particles while conserving the number of particles injected into the plume. Figure 4-5 gives the energy distributions for the cases of particles along the centerline and at 7.5° from the centerline, 0.6 m from the thruster exit. The run which neglected the effects of double ionization shows, on the average, that more particles are reaching the 0.6 m mark along the thruster centerline. In fact, the value of the percent difference between the numbers of particles sampled at the centerline is 48% on average and is 30% at the peak.

These results suggest that single ions hold straighter trajectories than double ions. Thus, when sampling at angles near the centerline, one can expect measuring the effect of single ions, while sampling at a greater divergence from the centerline yields the effects of the double ions. This is further substantiated by Figure 4-6 which compares the RPA data at angles further from the centerline.

Figure 4-7 shows the current density comparison at 0.6 m away from the thruster exit. As can be seen, there is a slight loss in current with less current seen at larger angles for the run without double ions present. This is due to the fact that the current is not conserved in the simulation. The average percent difference between the baseline and the run without double ions is 24%.

These results are only preliminary and give some indication of what would happen if double ions were not included in the plume. It is not the complete picture of what occurs physically.

Furthermore, the dominant collision phenomenon in the plume has been shown to be double-ion CEX collisions. A collision log was used to track collision statistics during the run of the plume code. For the baseline case, approximately 47% of all collisions were due to double-ion CEX ($Xe^{++}_{fast} + Xe_{slow} \rightarrow Xe_{fast} + Xe^{++}_{slow}$), while only 30% were from single-ion CEX. Consequently, a decrease in the number of double ions results in a decrease in the overall number of charge-exchange (CEX) collisions which occur in the plume. The result is less particle backflow towards the thruster. This decrease in backflow current is misleading in thruster–bus integration issues. Satellite designers would require an accurate estimate of plume and thruster assembly interactions in order to assess the reliability of the bus subsystem.

In addition, the surface interaction model may generate misleading results. One side of a solar array surface is given in Figure 4-8. Compared against the baseline case shown in Figure 4-9, the distribution of impinging particles on the surface in the case with double ions is slightly different than the distribution in the case which excludes double ions. Removing the double ions eliminates the erosion patch in the middle of the panel which is formed by double ion impingement in the baseline case.

4.1.4 Exit Plane Distribution

Automatic Source Model Generation

The ion current density and beam divergence angle distributions can be obtained from the automatic source generation code. However, the code must be used with a caveat. The grid used in the channel model is asymmetric in the plume region about the exit plane. As a result, the distributions generated from the output of the channel code are asymmetric as well. Curve fits to the distributions, such as the ion current density fit shown in Figure 4-10, are similarly skewed.

Figure 4-10 shows the skewed curve fit along with the data interpolated along the sampling line 4 mm from the thruster exit. Figure 4-11 displays the same data with one point removed. In order to generate an accurate description for the source, one must choose the data, by either a visual or an automatic cutoff technique, with caution.

However, since we are converting the ion current density distributions into a cumulative probability distribution function, we must investigate how the probability distribution changes with changes in the current density distribution. Figure 4-12 gives the probability distribution functions generated from the two ion current density distributions described above. The probability is slightly over predicted when using the skewed distribution for the ion current density. However, the largest difference between the two probability curves exists at a radius of approximately 0.032 m and has a value of between 0.035 and 0.05. Figure 4-13 shows the probability curves using a smaller range to exemplify this result. The probabilities are small enough that it is fair to say that a probability of occurrence of 0.035 is approximately the same as that of 0.05. The difference between the curves do not continue above approximately 0.2 in the probability distribution. Thus, the skewness seen in the distribution function is so slight that it will not have much effect on the output of the plume simulation.

Improvements to the automatic source generation code include incorporating dynamic memory allocation into the code for the arrays which are passed into the Numerical Recipes curve fit functions. When sampling at locations past the exit plane, no grid points exist from which to interpolate data at the lower bound of the grid. In finding the points which are closest to the given distance from the exit plane, z, the code searches along the radial grid lines to generate a set of 22 data points. Since the radial grid lines turn with the plume, there exist some gridlines which do not cross a certain distance z. Thus, the static memory allocated for the array holding the sampled data points is not filled and must be filled before going into the curve fit routines. Filling the array with extra points introduces error into the curve fits. The unwanted data points can be eradicated by dynamically allocating memory for the array as the data points are read. In a similar fashion, the data points which skew the distributions generated can also be removed before performing the curve fit routines.

Ultimately, the code could output a source (source.c) file for the plume model which includes the curve fits directly. The source file could be read and transferred to another file while inserting generated probability and beam divergence angle distributions at the proper locations.

Applications

Ion current density and beam divergence angle results from the acceleration channel code were sampled 4 mm from the thruster exit plane. The original experimental data, which are used in the Oh model, were taken 4 mm from the thruster exit plane by Gavryushin [12]. This was the closest distance from the exit plane such that the probe did not disturb the flow. The comparison between the simulated and experimental data is presented in Figures 4-14 and 4-15 as a function of thruster radius.

Figure 4-14 compares the ion current density distribution between the simulated and experimental cases. The automatic source generation code was used to extract the data. One data point was removed, and the fit was taken (see Figure 4-11). The curve for the experimental data is actually a fit to the data shown in Figure 3-1.

The figures show very good agreement between the acceleration channel code and the experimental data. The shift seen in the figure is due to the fact that two different thruster geometries were used to generate the ion current density distributions. Thus, the differences in the widths of the distributions are caused by differences in inner and outer radii of the thruster channel.

The cumulative distribution functions which were created from the the acceleration channel code and the experimental data are shown in Figure 4-16. The cumulative distribution function generated from the acceleration channel code under predicts at intermediate radii the function generated by experimental data. This reflects the shift of the Fife current to the outer radii (Figure 4-14). The ion current density data from the channel code was simply spread out over the larger channel width without changing the magnitude of the data.

Sensitivity to the two different source models using the erosion rate metric is given in Section 4.3.

4.2 Sputtering Model

When running the thruster simulations, satellite designers must have access to the interactions between the thruster and the spacecraft. Thus, enhancing the plume's existing sputtering model is of importance in the development of the complete end-to-end model.

The baseline satellite geometry used for sputtering analysis, shown in Figure 4-17, consists of a bus, yoke, and solar array. The thruster is mounted at a 45° cant angle and forms a 45° angle with the solar array. This geometry was chosen such that the results of the sputtering analysis were comparable to Dr. Oh's dissertation cases. All runs were for 10,000 iterations with a total of 15,825 particles striking all surfaces.

As discussed in Section 3.1.2, it has been shown that the maximum sputtering yield for most materials occurs between 60° and 80° [2]. The distribution of angle of incidence for the baseline case on all surfaces is given in Figure 4-18. The average incidence angle is 48.5°. Clearly, since a large number of particles are striking surfaces at non-normal angles of incidence, it is likely that the original sputtering model, which only included the effects of normally incident particles, under predicts the sputtering rates for the three materials investigated: silver, silicon, and quartz.

Figure 4-22 gives the sputtering rate for silver including the yield correction accounting for particle angle of impact. Compared against the sputtering rate without the angular dependence correction (Figure 4-9), the erosion rate seen with the correction is slightly larger. Here, the mean sputtering rate on all surfaces is 0.183 microns per month as opposed to the baseline rate of 0.177 microns per month. For the energies we are considering, the sputtering of silver is not significantly modified and could be given by the simple linear relationship for normal incidence.

However, this is not the case with silicon. The erosion rate using the correction, seen in Figure 4-23, is as much as four times the peak rate and three times the mean rate seen by normally incident particles.

The angular dependence correction to the sputtering yield was taken from the low-energy empirical model developed by Yamamura, Itikawa, and Itoh [25]. This model gave gave the most reasonable results for sputtering yield dependence on angle of incidence that could be found. The extension of Oh's sputtering model to include the angular dependence was constructed by introducing an angular dependence coefficient as a multiplier to the normal sputtering yield.

Values for f and Σ in Equation 3.5 are average values calculated from a set of data tables in Reference [25] for each element. Yamamura does not give a range for which the model is valid; however, the values for the sputtering correction were estimated for silver and silicon for energies of up to 1100 eV and for angles between 0° and 90° from the normal. It was found that the model gave "believable" results for xenon at energies above 50 eV sputtering silver and xenon above 200 eV sputtering silicon. The threshold energies for silver and silicon, respectively, are 26.38 eV and 95.24 eV. Particles with energies below 50 eV and 200 eV for silver and silicon, respectively, were taken to have no correction to the sputtering yield given by Oh [16].

A second data set serves to corroborate the Yamamura results and was also incorporated into the plume model. Empirical data were taken from Andersen and Bay [2] for a xenon ion striking molybdenum at 30 keV. The data were placed into a hashtable for ease of lookup. Computationally, the hashtable was the quickest implementation of the database. It is a form of a lookup table which reduces search time by breaking the data into buckets. Once the bucket is determined by an O(1) operation, a linear search is performed on that bucket to find the correct value based on a key. Thus, only one data file is necessary for each database one would like to store.

As a first approximation, the same sputtering data were used uniformly for all materials. This was done to test the sensitivity of the erosion rate to the changes introduced by the addition of the angular dependence. The Andersen and Bay data represent the worst-case considered, since high-energy incident ions increase sputtering yield by as much as a factor of six at angles between 70° and 80°. It does not, however, take into account energy dependence nor does it take into account material dependence.

The erosion rates for silver and silicon on the solar array surface facing the thruster for the Oh baseline model are given in Figures 4-9 and 4-19. The Andersen and Bay data results are shown in Figures 4-20 and 4-21. Clearly, the addition of the coefficient has significant implications for the erosion rate predictions. Once again, the erosion increased by factor of between four and five at the peak.

From Figures 3-6 through 3-8, it is clear that the Yamamura model appears to best predict the data in the few keV range for xenon projectiles. Once again, the solid line represents a fit to the data, while the cross-marked lined represents the model. Thus, we should expect below this range, the sputtering is under predicted, while over this range, the sputtering is over predicted.

To account for this, the sputtering correction values given by the model can be multiplied by another factor to increase the weighting of the curve so that we can compensate for the under prediction in the below 550 eV range, since the ions in the plume only exhibit energies between 0 and 400 eV.

However, it is not necessary at the moment to take this step, since recent experimental data needed to validate the results discussed above have not been available.

4.3 Sensitivity Analysis

A preliminary sensitivity analysis was conducted to determine the bounds to the domain of analysis shown in Figure 3-9. The four cases corresponding to the corners of the domain were evaluated. The Yamamura model comparison to the baseline was discussed in the sputtering section above. The results of the comparison between the other two corners, consisting the engine code (Fife model) with and without the inclusion of Yamamura model and the baseline case, are given below.

Figure 4-24 displays the erosion data using the engine code output as the source. Angular dependence in sputtering was not considered. Compared against the baseline given in Figure 4-9, considerable differences exits in both distribution of particles on surfaces as well as in the magnitude of erosion.

The same can be seen by comparing results from the baseline source model and the Fife source model, including the Yamamura sputtering model in both cases. Figures 4-25 and 4-26 give the sputtering of silver and silicon, respectively, using the Fife source model. The erosion rates seen are more localized and are approximately two and a half times higher at the peak than those seen in Figures 4-22 and 4-23. The mean values of the erosion rate on all surfaces are approximately three and a half times higher.

This magnitude difference can be explained by the number of particles striking the surfaces: using the Fife distribution, 19,490 particles struck the surface as opposed to 15,825 particles in the baseline case.

Clearly, the erosion metric is extremely sensitive to changes in the source model distributions. A thorough survey is necessary to fully quantify the sensitivity to the input distributions [18]. In addition, the erosion rate may not be the metric which should be chosen to compare input parameters' effects on the plume model. RPA data and ion current density distributions should be monitored for changes as well.

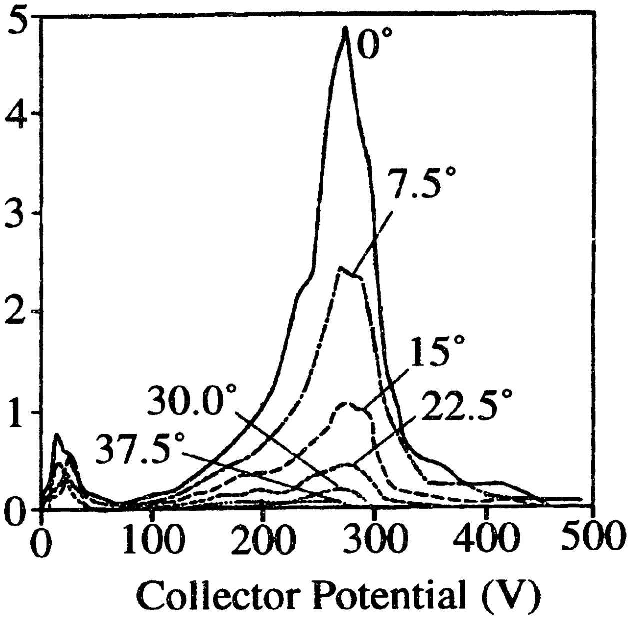

Figure 4-1: RPA energy distribution taken 1 m from thruster exit. [1]

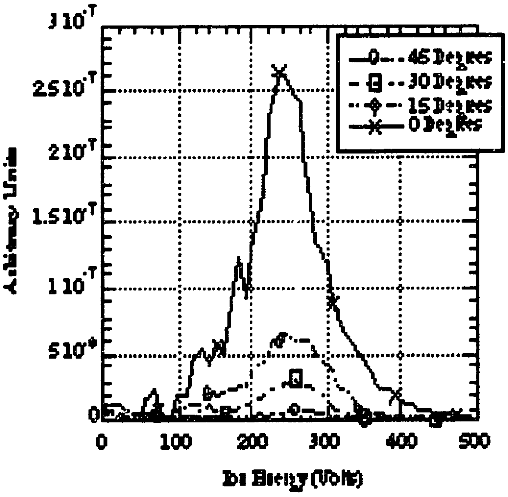

Figure 4-2: RPA energy distribution taken 50 cm from thruster exit. [Marrese/Gallimore] $P = 5.2 \times 10^{-5}$ Torr (Figure reprinted here for convenience.)

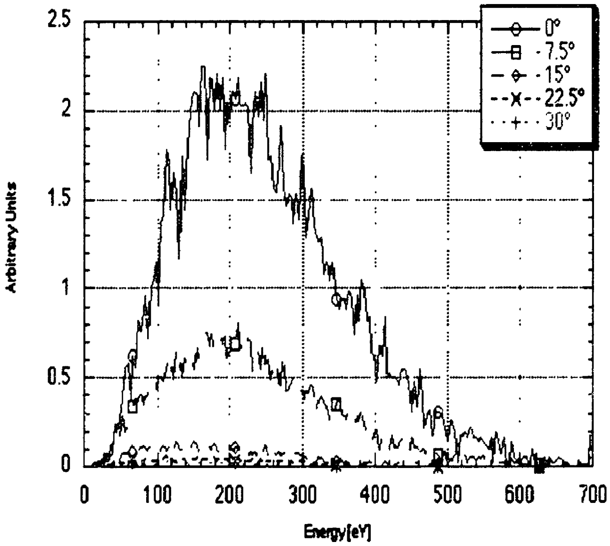

Figure 4-3: Simulated RPA energy distribution taken 60 cm from thruster exit. $T_i = 34.0$ eV, $P = 2.2 \times 10^{-6}$ Torr (Figure reprinted here for convenience.)

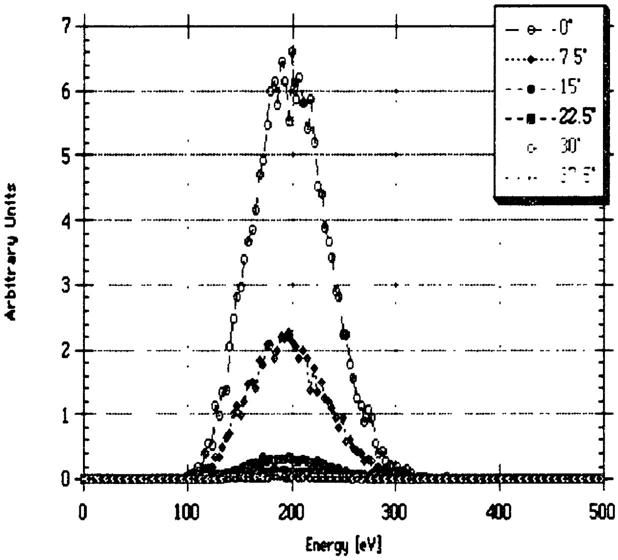

Figure 4-4: Simulated RPA energy distribution taken 60 cm from thruster exit. $T_i = 3.4$ eV, $P = 2.2 \times 10^{-6}$ Torr

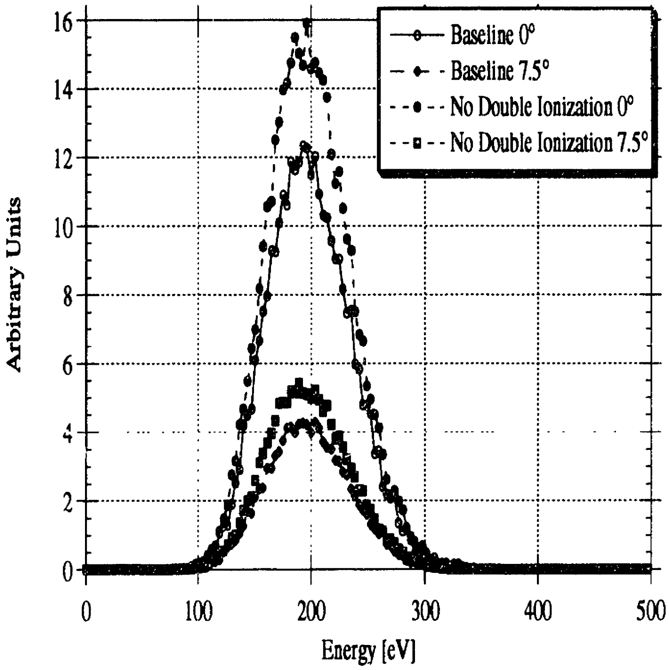

Figure 4-5: Comparison of simulated RPA data with and without double ionization. ($z = 0.6$ m)

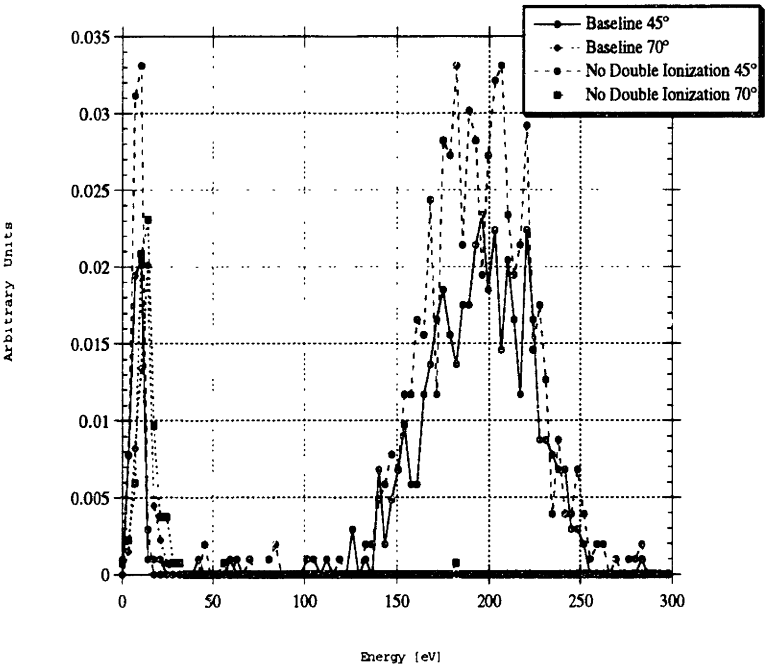

Figure 4-6: Comparison of simulated RPA data with and without double ionization at large angles from the thruster centerline. ($z = 0.6$ m)

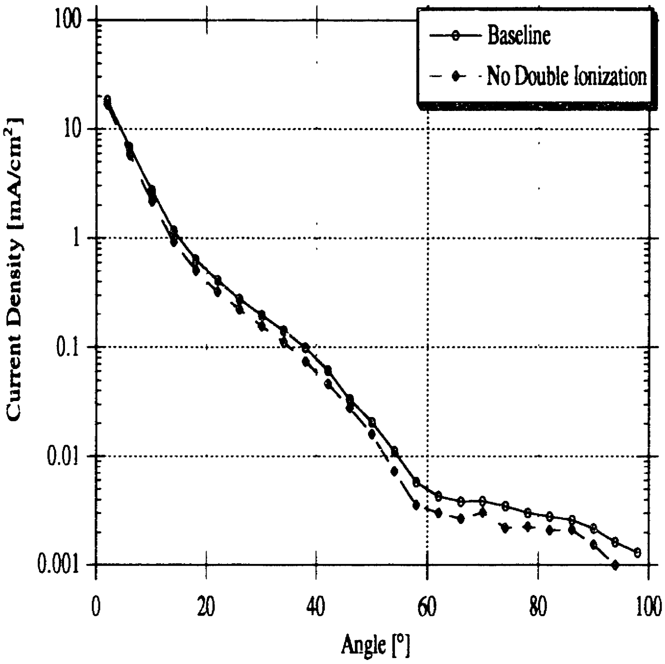

Figure 4-7: Comparison of simulated current density with and without double ionization. ($z = 0.6$ m)

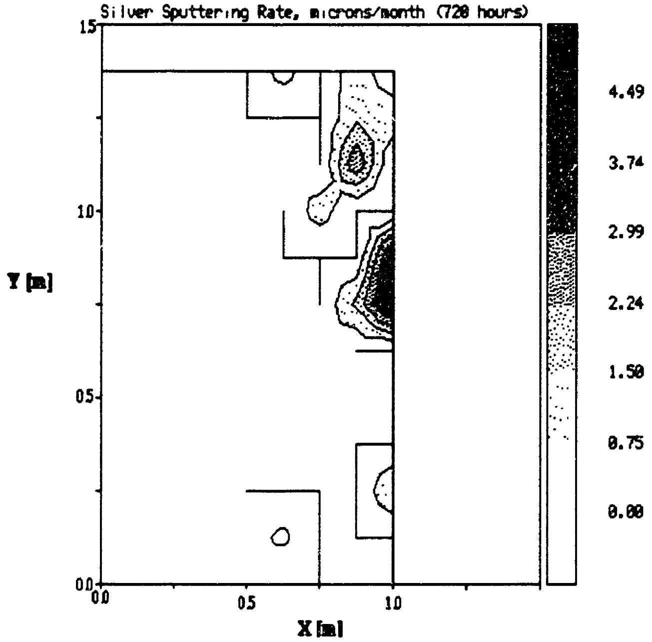

Figure 4-8: Sputtering of silver. Double ions not included.

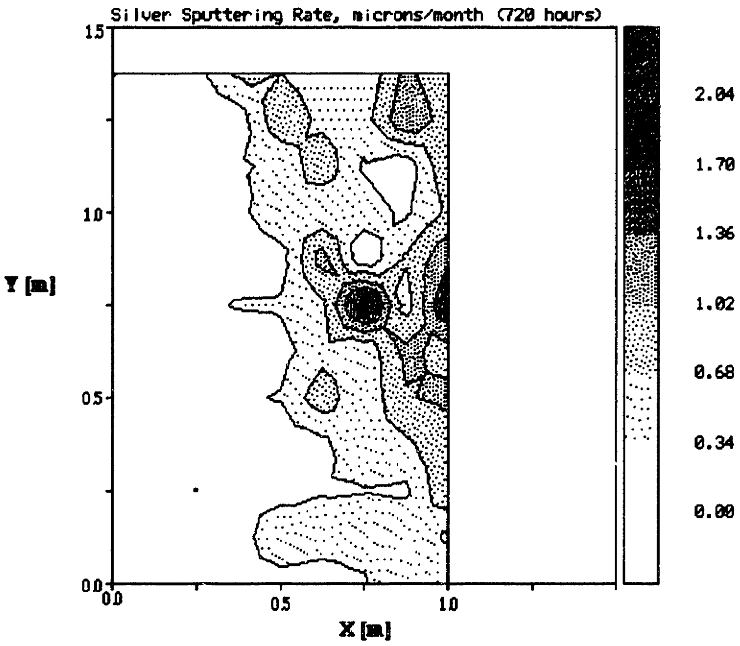

Figure 4-9: Baseline sputtering of silver.

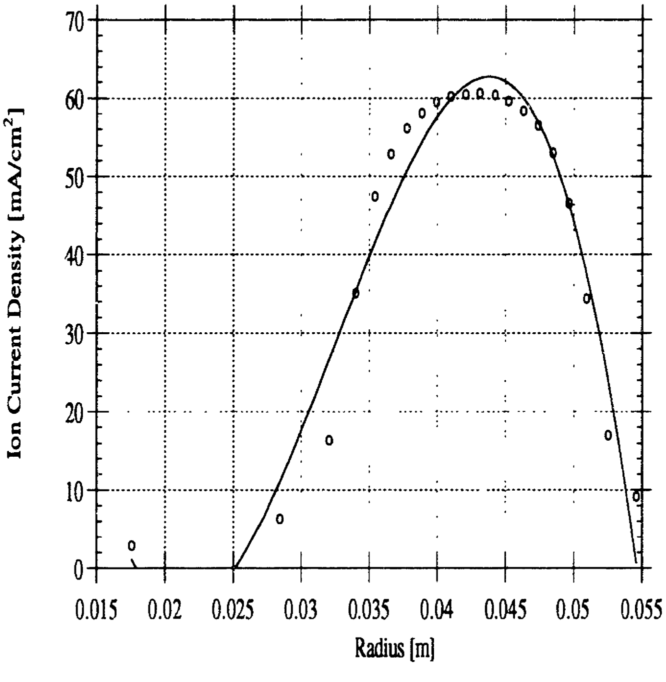

Figure 4-10: Curve fit of data sampled 4 mm from the exit plane.

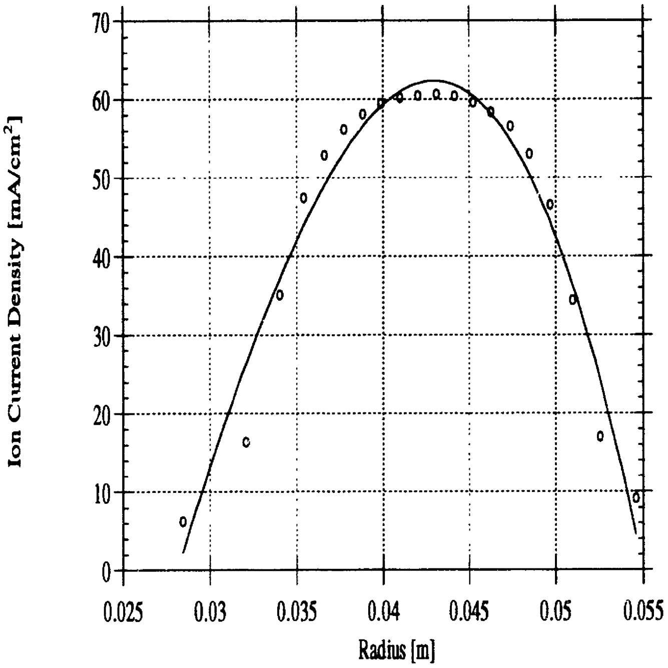

Figure 4-11: Curve fit of data sampled 4 mm from the exit plane minus one data point.

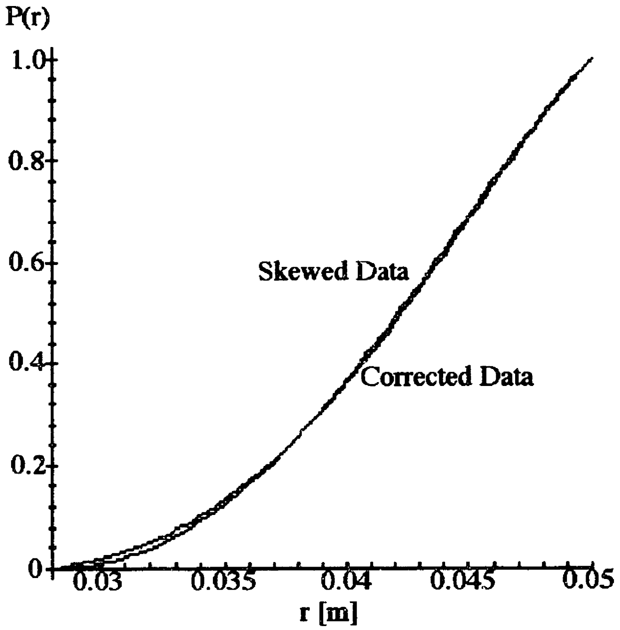

Figure 4-12: Cumulative distribution functions created from ion current density.

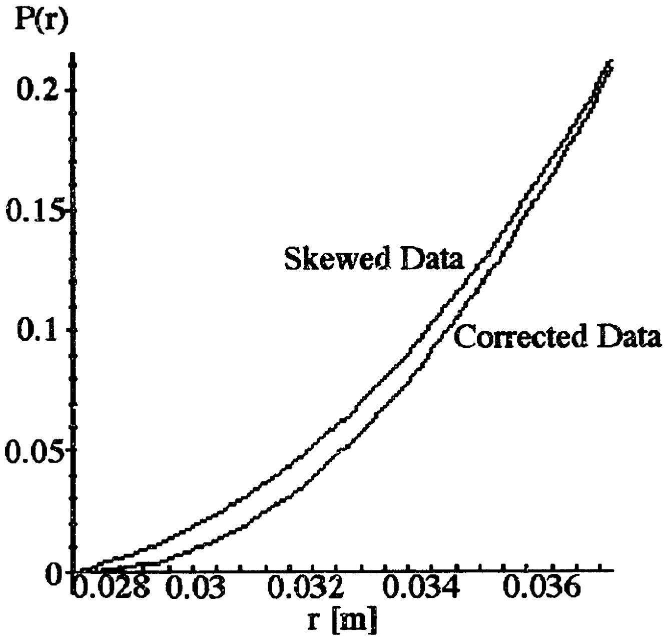

Figure 4-13: Cumulative distribution functions shown for $r = 0.028 - 0.037$ m.

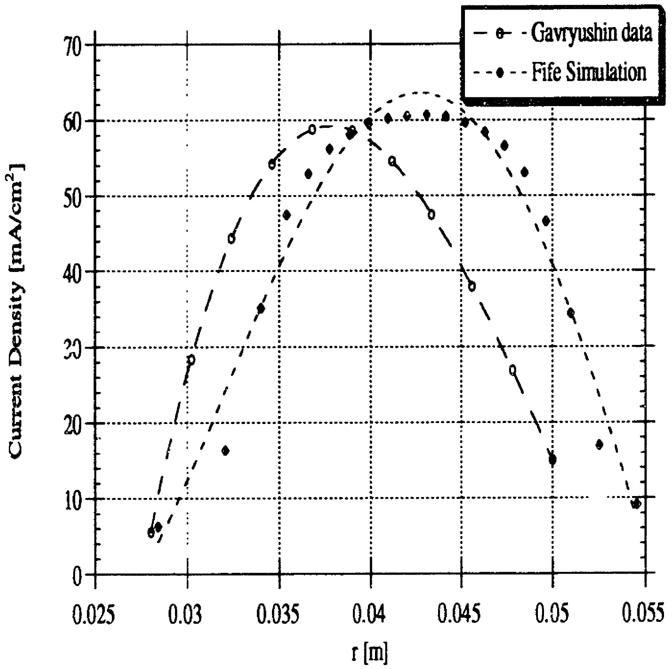

Figure 4-14: Comparison of Fife and Gavryushin ion current density distributions 4 mm from thruster exit.

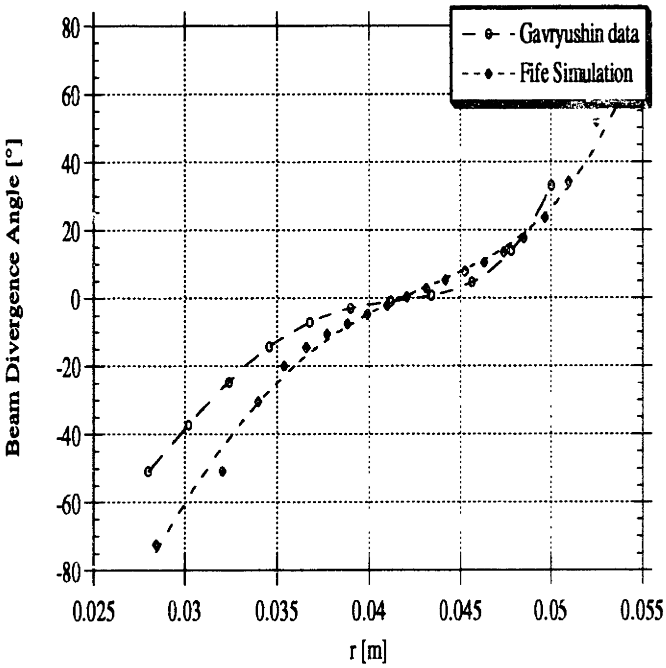

Figure 4-15: Comparison of Fife and Gavryushin beam divergence angle distributions 4 mm from thruster exit.

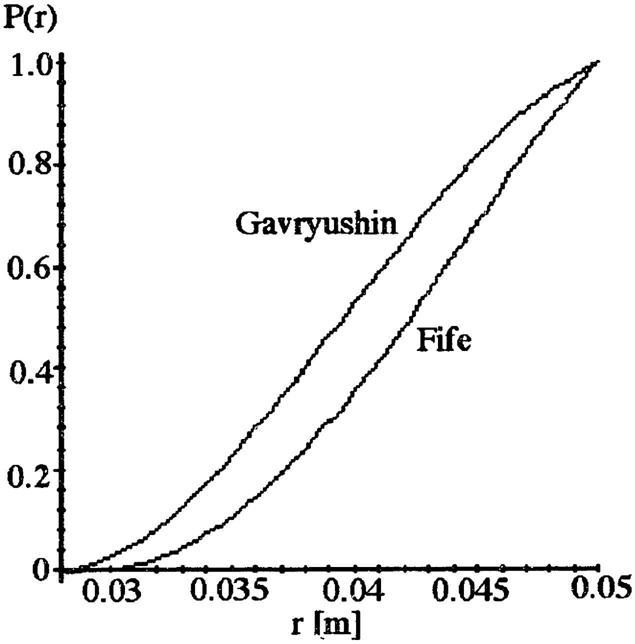

Figure 4-16: Comparison of Fife and Gavryushin cumulative distribution functions.

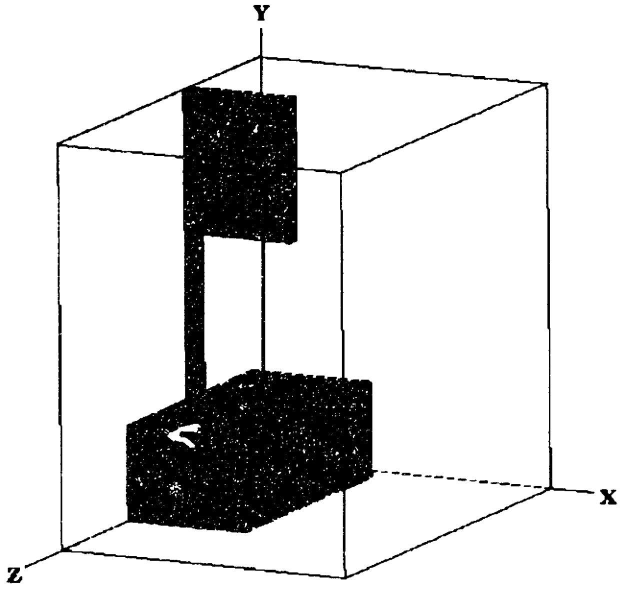

Figure 4-17: Baseline configuration of satellite. Includes bus, yoke, and array.

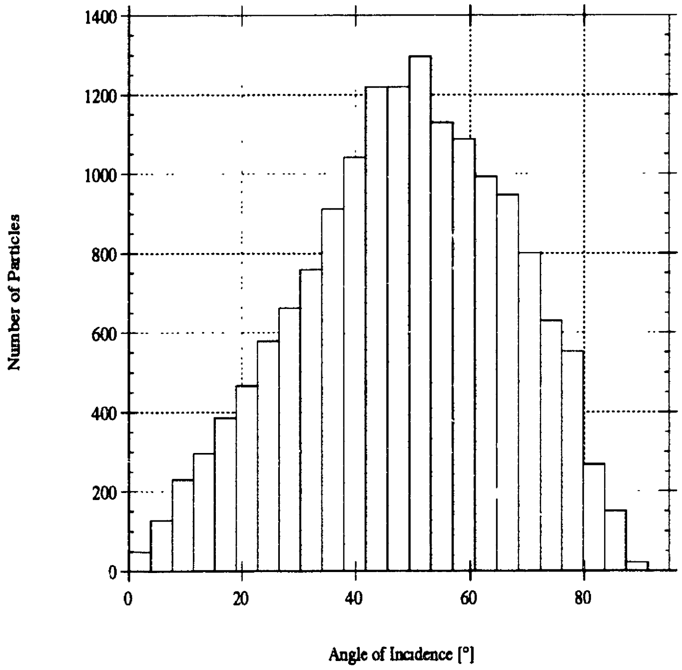

Figure 4-18: Distribution of angle of incidence on all surfaces of satellite.

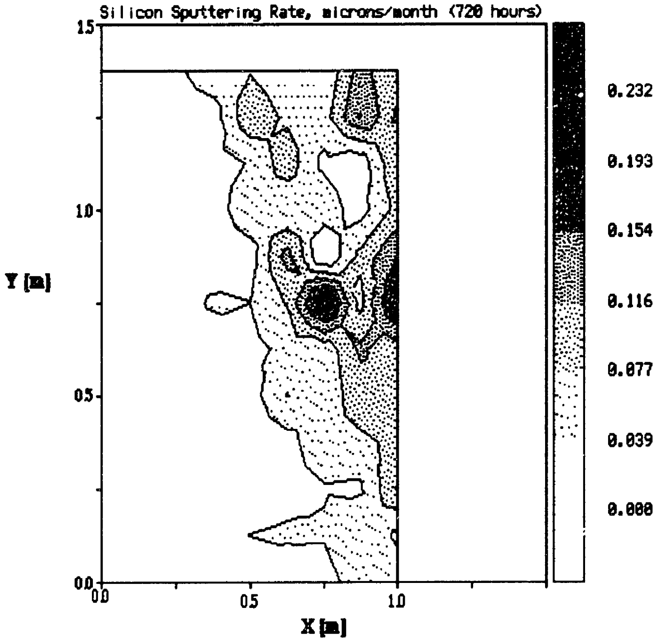

Figure 4-19: Baseline sputtering of silicon.

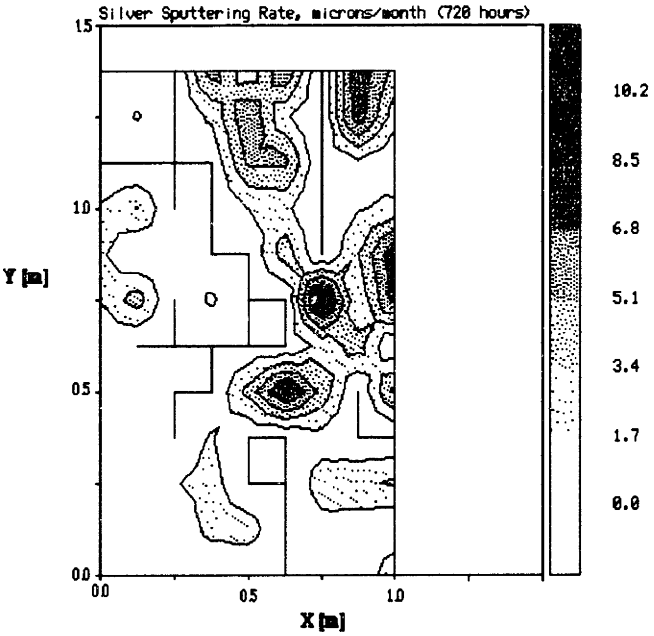

Figure 4-20: Worst-case sputtering of silver.

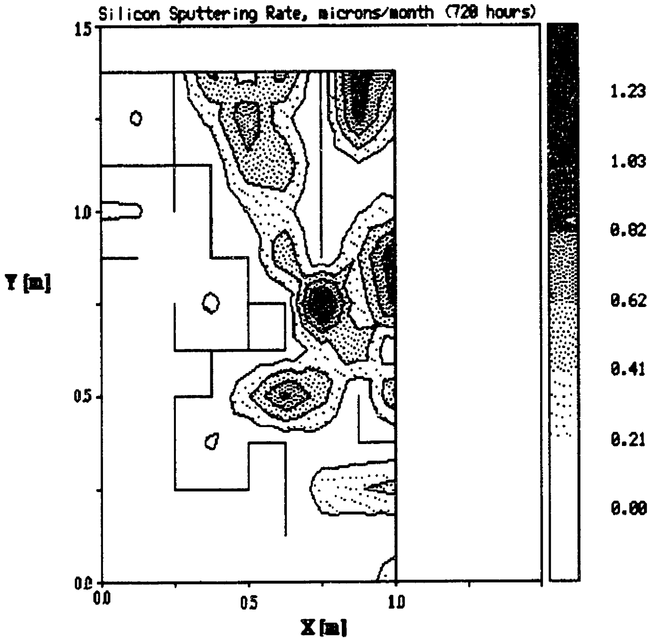

Figure 4-21: Worst-case sputtering of silicon.

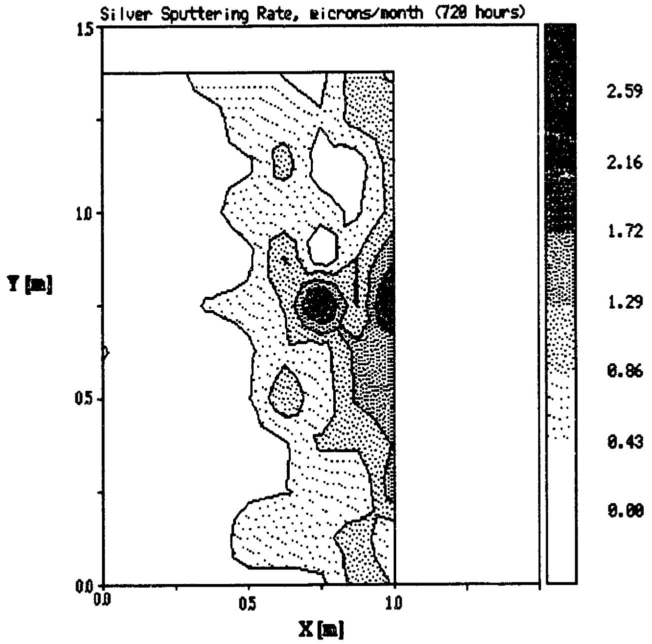

Figure 4-22: Sputtering of silver using Yamamura model for angle of incidence dependence.

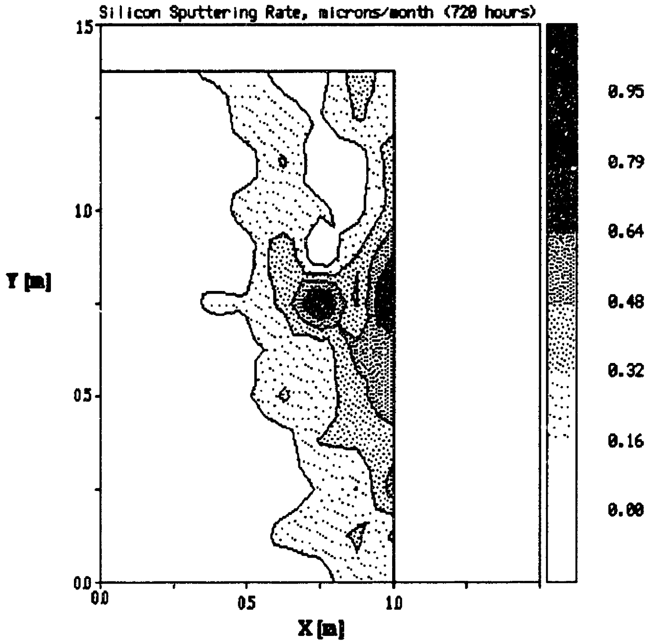

Figure 4-23: Sputtering of silicon using Yamamura model for angle of incidence dependence.

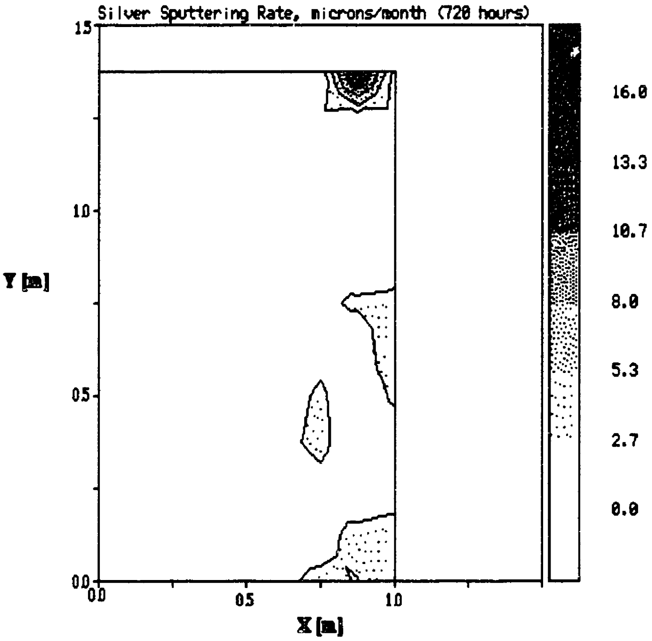

Figure 4-24: Sputtering of silver using Fife ion current density and beam divergence angle distributions 4 mm from exit. Sputtering angular dependence not included.

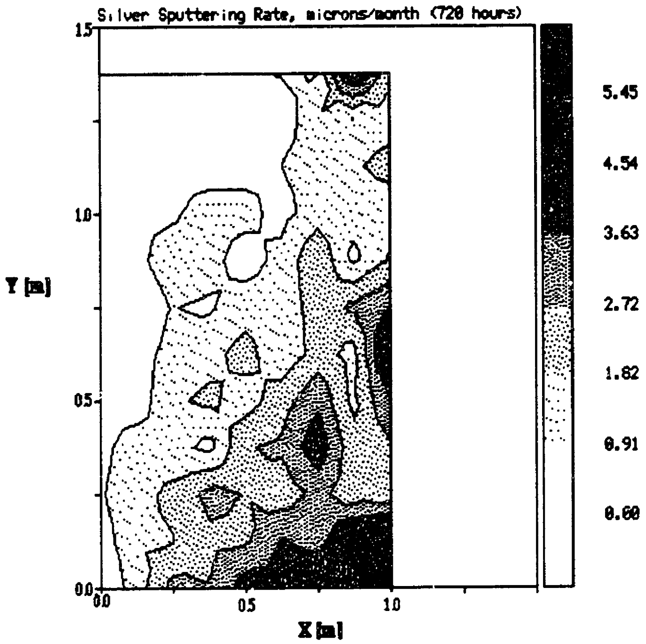

Figure 4-25: Sputtering of silver using Fife ion current density and beam divergence angle distributions 4 mm from exit. Sputtering angular dependence is included.

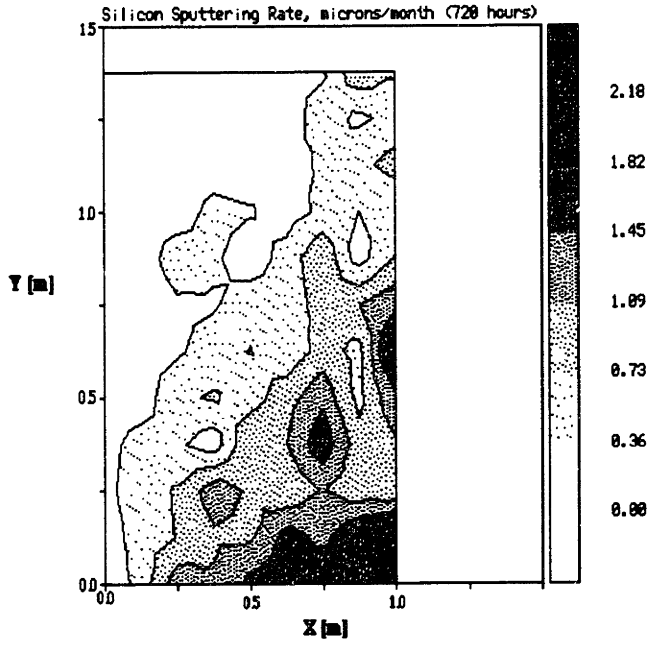

Figure 4-26: Sputtering of silicon using Fife ion current density and beam divergence angle distributions 4 mm from exit. Sputtering angular dependence is included.

Chapter 5

Conclusions

Issues regarding the generation of a complete computational model of a Hall thruster have been evaluated. These include the modeling of plasma oscillations and double ions, enhancements to the original three-dimensional PIC-DSMC plume code, and the evaluation of the sensitivity of plume code to relevant source models. The next section summarizes results and presents the conclusions drawn from the results of the work. The following section presents the recommendations for the generation of an integrated model.

5.1 Summary of Results

The results of the work are presented below.

- Ion Energy Discrepancy

  The discrepancies between the RPA data in the original plume model by Oh and that found in experiment have been determined to be related to the axial ion temperature assumed in the plume model. Increasing the axial ion temperature at the source increases the thermal velocity which acts to keep the particle along the centerline. The peak in the distribution of energies shifts with higher energy particles due to the inflated temperature. Furthermore, the high energy seen in the simulated data is lost as the axial ion temperature is decreased at the source.

- Double Ions

  Xenon double ion and neutral CEX is the dominant collision process in the plume. The removal of double ions decreases the number of CEX collisions which occur. This has clear implications on the plume character.

- Sputtering Model Enhancement

  A correction to the yield rate of normally incident ions to account for non-normal angles of impact was implemented. As a result, erosion rates seen on simulated spacecraft surfaces increased by up to a factor of four. This represents a significant enhancement of the original sputtering model.

- Sensitivity

  An erosion metric was used to gauge the sensitivity of the plume model to various source inputs. The metric was found to be extremely sensitive to changes in the source model ion current density and beam divergence angle distributions.

Based on these results, the following conclusions have been drawn:

- An accurate source model is critical to the proper operation of the plume code. Thus, double ions should be incorporated into the acceleration channel model. Without the double ions, incorrect conclusions may be drawn concerning back-flow current and erosion rates.

- The sensitivity of the plume model to various source inputs should also be statistically investigated.

- Resolving plasma oscillations using the current plume model may be infeasible. Preliminary results indicate that the time step necessary to resolve the oscillations increases the total running time of the code over 10 times. Currently, the plume code takes approximately four hours to run on an SGI Octane (dual R10000 175 MHz processors) for 10,000 iterations. More serious, however, may be the problem of needing more particles per cell.

- Sputtering of silicon is heavily dependent on angle of incidence of impinging particles. Silver sputtering is not significantly modified by corrections to the yield rate to include the angular dependence. Data for the angular dependence of quartz sputtering should be incorporated into the plume model they become available.

- Good statistics can be generated with the plume model when satisfying three necessary conditions:

  1. The time step should be small enough to resolve all processes of interest.
  2. There must be enough particles per cell at locations of interest.
  3. Although a steady-state total energy is reached after 3000 iterations, the run time for the code should be 10,000 iterations or greater to generate smooth erosion data.

5.2 Short-Term Recommendations

5.2.1 Source Model

The automatic source generation code should be streamlined to include dynamic memory allocation. A point selection-rejection routine should also be added to generate more accurate distributions at the sampling locations.

Plasma oscillations should be included if EMI and signal interference are to be studied with the model. However, contamination and deposition could more easily be incorporated. It has been shown that contamination is a problem at high angles from thruster exit [21]. We should concentrate efforts on explaining this, since these issues would be much more tractable for the near future than the oscillations.

5.2.2 Sputtering Model

The assumption of ideal specular reflection is for neutrals hitting the surfaces is not quite true. This portion of the plume code should be changed in order to take into account accommodation and various sputtering regimes.

5.2.3 Integration

Integration in the short-term shall consist of first running the acceleration channel code to convergence and then inputting the data into the plume model. Validation can be achieved upon the full validation of the individual parts. The total running time of the code would be 8 hours on an SGI Octane. The source model for the plume code must be completely derived from the output of the acceleration channel code. This is a substantial task which requires identifying the parameters necessary and automatically finding the parameters from the output. Thus far, the automatic generation code consists of parsing only the ion flux data to create the distributions of the ion current density and beam divergence angle.

5.3 Long-Term Recommendations

In the long-term, the two models would have to be combined seamlessly. However, this does not seem feasible from the time stepping constraints. The time steps which the acceleration channel code uses is two orders of magnitude smaller than that of the plume model. Thus, the amount of time necessary for convergence and the generation of good statistics would be on the order of hundreds of hours. This issue of time step should be investigated in much more detail.

Additionally, the mesh on which the plume model resides must be reconstructed to match the engine code for a seamless integration. This would require a reconstruction of the algorithms used in the plume model to take into account the unstructured mesh.

5.4 Summary

In closing, two- and three-dimensional computational models describing both the internal and external physics of Hall thrusters have been developed at the Massachusetts Institute of Technology. Integration of these models would result in a single, stand-alone application characterizing thruster physics from the thruster interior through the plume region. The application would enhance the spacecraft design process by providing engineers with the ability to predict thruster performance and damage to the craft from plume-spacecraft interactions.

The two models can be combined; however, a large amount of reconstruction may be needed for seamless integration. If seamless integration is unnecessary, the short-term solution of using the time-averaged results of one to generate the input to the other is sufficient.

Bibliography

[1] Absalamov, S.K., V.B. Andreev, et al. AIAA Paper 92-3156, "Measurement of Plasma Parameters in the Stationary Plasma Thruster (SPT-100) Plume and Its Effect of Spacecraft Components." July 1992.

[2] Andersen, H.H. and H.L. Bay. "Sputtering by Particle Bombardment I: Sputtering Yield Measurements." *Topics in Applied Physics*, 47:200–203, 1981.

[3] Behrisch, R. "Sputtering by Particle Bombardment I: Introduction and Overview." *Topics in Applied Physics*, 47, 1981.

[4] Birdsall, C.K. and A.B. Langdon. Plasma Physics Via Computer Simulation. McGraw–Hill Book Company: New York, 1994, Second ed.

[5] Bishaev, A.M, and V. Kim, "Local Plasma Properties in a Hall-Current Accelerator with an Extended Acceleration Zone," *Soviet Physics Technical Physics*, 23(9):1055–1057, 1978.

[6] Covault, C. "Hughes Satcom Surge Advances Propulsion." *Aviation Week and Space Technology.* 147(24):70, 1997.

[7] Crofton, M.W. Evaluation of Electric Thrusters. Aerospace Report ATR-97(8201)-1, The Aerospace Corporation, El Segundo, CA, April 15, 1997.

[8] Duchemin, O.B., J.R. Brophy, C.E. Garner, P.K. Ray, V. Shutthanandan, and M.A. Mantenieks. IEPC Paper 97-068. "Review of Low Energy Sputtering Theory and Experiments." 25th International Electric Propulsion Conference, Cleveland, OH, August 24–28, 1997.

[9] Fife, J.M. *Two-Dimensional Hybrid Particle-In-Cell Modeling of Hall Thrusters.* S.M. Thesis, Massachusetts Institute of Technology, Department of Aeronautics and Astronautics, May 1995.

[10] Fife, J.M. *Two-Dimensional Hybrid Particle-In-Cell Modeling of Hall Thrusters.* Doctoral Thesis in Progress, Massachusetts Institute of Technology, Department of Aeronautics and Astronautics, 1998.

[11] Fife, J.M., M. Martinez-Sanchez, and J. Szabo. AIAA Paper 97-3052. "A Numerical Study of Low-Frequency Discharge Oscillations in Hall Thrusters." 33rd AIAA/ASME/SAE/ASEE Joint Propulsion Conference & Exhibit, Seattle, WA, July 6–9, 1997.

[12] Gavryushin, V.M., and V. Kim. "Effect of the Characteristics of a Magnetic Field on the Parameters of an Ion Current at the Output of an Accelerator with Closed Electron Drift." *Soviet Physics Technical Physics*, 26(4):505–507, April 1981.

[13] Lentz, C.A. *Transient One Dimensional Numerical Simulation of Hall Thrusters.* S.M. Thesis, Massachusetts Institute of Technology, Department of Aeronautics and Astronautics, September 1993.

[14] Manzella, D.H. IEPC Paper 93-097, "Stationary Plasma Thruster Plume Emissions." 23rd International Electric Propulsion Conference, Seattle, WA, September 13–16, 1993.

[15] Mitchner, M. and C.H. Kruger, Jr. Partially Ionized Gases. John Wiley & Sons, Inc.: New York, 1973.

[16] Oh, D.Y. *Computational Modeling of Expanding Plasma Plumes in Space Using a PIC-DSMC Algorithm.* Sc.D. Thesis, Massachusetts Institute of Technology, Department of Aeronautics and Astronautics, February 1997.

[17] Press, W.H., S.A. Teukolsky, W.T. Vetterling, and B.P. Flannery. Numerical Recipes in C. Cambridge University Press: Cambridge, UK, 1992 ed.

[18] Qarnain, S. and M. Martinez-Sanchez. TBP AIAA Paper 98-3796, "Issues Regarding the Generation of an End-to-End Hall Thruster Computational Model." 34th AIAA/ASME/SAE/ASEE Joint Propulsion Conference & Exhibit, Cleveland, OH, July 13–15, 1998.

[19] Randolph, T. and R. Burton. "The Year in Review: Electric Propulsion." *Aerospace America*, December 1997.

[20] Randolph, T., E. Pencil, and D. Manzella. AIAA Paper 94-2855, "Far-Field Plume Contamination and Sputtering of the Stationary Plasma Thruster." 30th AIAA/ASME/SAE/ASEE Joint Propulsion Conference, Indianapolis, IN, June 27–29, 1994.

[21] Sankovic, J., L. Cavney, and P. Lynn. AIAA Paper 97-2917. "The BMDO Russian Hall Thruster Technology (RHETT) Program: From Laboratory to Orbit." 33rd AIAA/ASME/SAE/ASEE Joint Propulsion Conference & Exhibit, Seattle, WA, July 6–9, 1997.

[22] Sigmund, P. "Theory of Sputtering, I. Sputtering Yield of Amorphous Solids and Polycrystalline Targets." *Physics Review*, 1842:383, 1969.

[23] Sutton, G.P. Rocket Propulsion Elements. John Wiley & Sons, Inc.: New York, 1992, Sixth ed.

[24] Szabo, J. Personal communication.

[25] Yamamura, Y., Y. Itikawa, and N. Itoh. IPPJ-AM-26, "Angular Dependence of Sputtering Yields of Monatomic Solids." Institute of Plasma Physics, Nagoya University, June 1983.

THESIS PROCESSING SLIP

FIXED FIELD: ill ______ name ______

index ______ biblio ______

▶ COPIES [✓ Archives] [✓ Aero] Dewey Eng Hum

Lindgren Music Rotch Science

TITLE VARIES ▶☐ ______

NAME VARIES: ▶☐ ______

IMPRINT (COPYRIGHT) ______

▶ COLLATION: 70 l

▶ ADD. DEGREE: ______ ▶ DEPT.: ______

SUPERVISORS: ______

NOTES:

cat'r: date

page: ▶ J156

▶ DEPT Aero

▶ YEAR 1998 ▶ DEGREE M.S.

▶ NAME QARNAIN, Salma